Pluto's Beating Heart Regulates the Atmospheric Circulation: Results From High-Resolution and Multiyear Numerical Climate Simulations

T. Bertrand, F. Forget, O. White, B Schmitt, S. Stern, H. Weaver, L. Young, K. Ennico, C. Olkin

JOURNAL OF GEOPHYSICAL RESEARCH, VOL. ???, XXXX, DOI:10.1002/,

Pluto's beating heart regulates the atmospheric circulation: results from high resolution and multi-year numerical climate simulations

T. Bertrand[1], F. Forget[2], O. White[1], B. Schmitt[3], S. A. Stern[4], H. A. Weaver[5], L. A. Young[4], K. Ennico[1], C.B. Olkin[4], and the New Horizons Science Team

Corresponding author: T. Bertrand, National Aeronautics and Space Administration (NASA), Ames Research Center, Space Science Division, Moffett Field, CA 94035, USA (tanguy.bertrand@nasa.gov)

[1]National Aeronautics and Space

Key Points.

- High-resolution simulations of Pluto's climate show that the circulation is dominated by $\sim$10 m s^{-1} retrograde winds during most of the year
- Nitrogen condensation-sublimation flows in Sputnik Planitia are creating an intense western boundary current.
- Atmospheric heat flux, transport of tholins and albedo feedbacks could explain the albedo contrasts observed in Sputnik Planitia.

Administration (NASA), Ames Research Center, Space Science Division, Moffett Field, CA 94035, United States

[2]Laboratoire de Métórologie Dynamique, IPSL, Sorbonne Universits, UPMC Univ Paris 06, CNRS, 4 place Jussieu, 75005 Paris, France

[3]Université Grenoble Alpes, CNRS, Institut de Planétologie et Astrophysique de Grenoble, Grenoble F-38000, France

[4]Southwest Research Institute, Boulder, CO 80302, United States

[5]Johns Hopkins University Applied Physics Laboratory, Laurel, MD, 20723, United States

Abstract. Pluto's atmosphere is mainly nitrogen and is in solid-gas equilibrium with the surface nitrogen ice. As a result, the global nitrogen ice distribution and the induced nitrogen condensation-sublimation flows strongly control the atmospheric circulation. It is therefore essential for Global Climate Models (GCMs) to accurately account for the global nitrogen ice distribution in order to realistically simulate Pluto's atmosphere. Here we present a set of new numerical simulations of Pluto's atmosphere in 2015 performed with a GCM using a 50-km horizontal resolution ($3.75° \times 2.5°$) and taking into account the latest topography and ice distribution data, as observed by the New Horizons spacecraft. In order to analyze the seasonal evolution of Pluto's atmosphere dynamics, we also performed simulations at coarser resolution ($11.25° \times 7.5°$) but covering three Pluto years. The model predicts a near-surface western boundary current inside the Sputnik Planitia basin in 2015, which is consistent with the dark wind streaks observed in this region. We find that this atmospheric current could explain the differences in ice composition and color observed in the north-western regions of Sputnik Planitia, by significantly impacting the nitrogen ice sublimation rate in these regions through processes possibly involving conductive heat flux from the atmosphere, transport of dark materials by the winds and surface albedo positive feedbacks. In addition, we find that this current controls Pluto's general atmospheric circulation, which is dominated by a retro-rotation, independently of the nitrogen ice distribution outside Sputnik Planitia. This ex-

otic circulation regime could explain many of the geological features and longitudinal asymmetries in ice distribution observed all over Pluto's surface.

1. Introduction

Among the most striking observations of Pluto, made by the cameras aboard New Horizons during the July 2015 flyby, is a planetary-scale multi-km-thick equatorial N_2-rich ice sheet (mixed with small amounts of CO and CH_4), covering the floor of the Sputnik Planitia basin that extends between latitudes 25°S-50°N at a level 3 km below the surrounding terrains [Stern et al., 2015; Grundy et al., 2016; Schenk et al., 2018]. Highlands to the east of this structure are also covered by N_2-rich ices, which merge with the ices of Sputnik Planitia through several valley glaciers [Protopapa et al., 2017; Schmitt et al., 2017; Howard et al., 2017]. Both regions form the left and right lobe of the heart-shaped Tombaugh Regio, likely the most active geological region on Pluto. Other observed reservoirs of N_2-rich ice include northern mid-latitudinal deposits mainly concentrated in local depressions, while CH_4-rich ice has been detected around the north pole and at the equator where it forms the massive "Bladed Terrain" deposits [Moores et al., 2017; Moore et al., 2018] and at the northern fringe of Cthulhu Macula.

Volatile transport models have been able to simulate the cycle of N_2 and CH_4 over different timescales and understand to first order the observed distribution of these ices across Pluto's surface [Hansen and Paige, 1996; Young, 2013; Toigo et al., 2015; Bertrand and Forget, 2016]. In particular, it has been shown that N_2 ice tends to accumulate in Sputnik Planitia due to its low elevation corresponding to a higher pressure and condensation temperature [Bertrand and Forget, 2016]. Outside the basin, observed latitudinal bands of N_2 and CH_4 deposits were reproduced by models (to first order) and shown to be related to the seasonal and astronomical cycles [Protopapa et al., 2017; Bertrand et al., 2018, 2019]. However, some of the observed longitudinal asymmetries in ice distribution, composition, texture or color could not be explained by these models. For instance, the equatorial regions west of Sputnik Planitia are volatile-free and covered by a dark mantle of organic materials (tholins), while the regions east of Sputnik Planitia are covered by N_2-rich and CH_4-rich ices, including the Bladed Terrain deposits which extend between 210°E and 40°E [Moore et al., 2018]. If the accumulation of CH_4 ice is predicted in the equatorial regions [Bertrand et al., 2019], this asymmetry in longitude remains a mystery. Another example is Sputnik Planitia's ice sheet itself, which displays bright and dark N_2 ice plains, the latter being enriched in dak red material and in CH_4 ice and located in the northern and western regions of Sputnik Planitia (see Fig. 35 and 36 in Schmitt et al. [2017] and Fig. 5 in Protopapa et al. [2017]).

Runaway albedo and volatile variations as well as differential condensation and sublimation have been suggested to explain these features [White et al., 2017; Moore et al., 2018; Earle et al., 2018], but the role of atmospheric circulation may be crucial and remains to be explored. Besides, the observations of wind streaks and eolian linear dunes on Pluto's surface [Stern et al., 2015; Telfer et al., 2018] are indications that Pluto's atmospheric dynamics can impact the surface geology.

Previous GCM modeling studies investigated the dynamics of the 1-Pa atmosphere of Pluto in 2015 and showed how near-surface winds (below 1000 m altitude) and the general circulation are controlled by the topography and the N_2 condensation-sublimation flow [Toigo et al., 2015; Forget et al., 2017]. In particular, Forget et al. [2017] used a post-New Horizons version of the Pluto GCM developed at the Laboratoire de Métórologie Dynamique (LMD), and performed a comprehensive characterization of the dynamics within

Pluto's atmosphere (wind regimes, waves, cloud formation, temperatures etc.). They showed that down-slope katabatic winds dominate everywhere across Pluto, as a result of surface temperatures being much colder than those in the atmosphere. At locations close to N_2 ice deposits, katabatic winds may be balanced during daytime by N_2 sublimation flows, and strengthened during nighttime by condensation flows.

Forget et al. [2017] highlighted the sensitivity of the general circulation to the atmospheric transport of N_2 and therefore to the locations of the sources and sinks of N_2 on the surface. They obtained three different dynamical circulation regimes for 2015, depending on the initial location of the N_2 ice deposits: (1) If N_2 ice was placed in Sputnik Planitia and on the poles, they predicted a retro-rotation, induced by conservation of angular momentum as N_2 is transported from one hemisphere to another, as also found by Toigo et al. [2015]. (2) If N_2 ice was placed in Sputnik Planitia and at the south pole, then the model predicted an intense condensation flux at the south pole leading to the formation of a prograde jet at high altitude, and, through mechanisms of wave instabilities, to a zonal circulation characterized by a super-rotation, like on Venus and Titan. (3) Lastly, if N_2 ice was placed in Sputnik Planitia only, the zonal winds obtained were weak and induced by a thermal gradient between both hemispheres. However, in this first low-resolution version of the LMD Pluto GCM, the Sputnik Planitia basin was represented as a simple circular crater located north of the equator. In reality, the Sputnik Planitia basin and ice sheet extend southward down to 25°S. This should trigger significant cross-equatorial transport of N_2 and impact the general atmospheric circulation.

Here we run higher resolution simulations of Pluto's atmosphere using the latest version of the LMD Pluto GCM coupled with New Horizons topography data. Our primary purpose is to describe the general circulation of Pluto's atmosphere in 2015, detail the near-surface circulation within Sputnik Planitia and provide explanation for some observations made by New Horizons, which will complement the work of Forget et al. [2017]. Section 2 presents the models and the methods used to reach consistent equilibrated atmosphere and surface conditions in the GCM. It also includes a description of the set of simulations used in this paper, which differ by their initial surface N_2 ice distribution. We present the model results in two different sections. Section 3 describes the near-surface circulation in Sputnik Planitia and compares the results with the available observations, whereas Section 4 describes the general circulation obtained for 2015. We also present preliminary results of a GCM simulation extending over three Pluto years. We discuss further these results and their implications on Pluto's climate in Section 5.

2. Model description

Our analysis was performed using the LMD three-dimensional GCM of Pluto [Forget et al., 2017; Bertrand and Forget, 2017] which includes atmospheric dynamics and transport, turbulence, radiative transfer, molecular conduction as well as phases changes for N_2, CH_4 and CO.

2.1. Recent improvements of the GCM

The model has recently been improved and now takes into account: (1) A digital elevation model (DEM) of the encounter hemisphere derived from New Horizons stereo imaging [Schenk et al., 2018]. We use flat topography for most of the non-observed hemisphere (see Section 2.3) as well as for the southern non-illuminated polar region (note that this has no impact on the results of this paper). (2) The presence of perennial CH_4-rich deposits in the equatorial regions (Bladed Terrains). On Pluto, these terrains are characterized by a high elevation (above 2 km), parallel sets of "blades" (steep ridges and sharp crests) and a relatively dark albedo [0.5-0.6 Buratti et al., 2017]. They are visible in the Tartarus Dorsa region (east of Sputnik Planitia) but their distinctive CH_4 absorption is seen in low resolution coverage of Pluto obtained during the New Horizons approach phase, suggesting that Bladed Terrain may occur in patches further east along the equator [Olkin et al., 2017; Moore et al., 2018]. In the model, we place a CH_4 ice reservoir at the locations of these terrains (inexhaustible over the timescales considered in this paper) with a topography similar to that of the resolved Bladed Terrains in Tartarus Dorsa. (3) A dual surface albedo for CH_4 ice: we use a CH_4 ice albedo of 0.5 for the equatorial deposits and an albedo between 0.65-0.75 for the polar CH_4 deposits (see Section 2.3), based on albedo maps of Pluto [Buratti et al., 2017].

2.2. General setting, initial and boundary conditions

Because Pluto orbits far from the Sun, its seasonal cycle is much longer than on Earth (one Pluto year is ∼248 Earth years). Above all, Pluto receives very little energy, which results in low sublimation-condensation rates and slow surface processes. This is an issue for Pluto GCMs because the simulations need to be performed over many Pluto years in order to be insensitive to the initial state. To solve this issue and obtain a physically self-consistent, equilibrated combination of initial surface conditions for the GCM (soil temperatures, ice distributions), we use the 2D LMD volatile transport model (VTM) of Pluto [Bertrand and Forget, 2016], and create an initial state for the GCM which is the result of 30 million years of volatile ice evolution, with N_2 ice filling and flowing inside

Sputnik Planitia [Bertrand et al., 2018, 2019]. A similar method has been used by Forget et al. [2017] and Toigo et al. [2015].

The radiative constant for Pluto's atmosphere, i.e. the time needed by the atmosphere to respond to a radiative forcing, is typically 10-15 Earth years [Strobel et al., 1996; Forget et al., 2017]. Therefore we start our 3D GCM simulations in 1984, so that the atmosphere reaches a realistic regime in 2015, insensitive to the initial state. The long-term VTM simulations and the low resolution GCM simulations are carried out with a horizontal grid of 32×24 points to cover the globe (i.e. 11.25° × 7.5°, ∼ 150 km in latitude) and 27 vertical levels (the altitude of the first mid-layers are 5 m, 12 m, 25 m, 40 m, 80 m and the model top is at 250 km). The years 2014 and 2015 are then simulated at a higher spatial resolution by using a grid of 96×72 points (3.75°×2.5°, ∼ 50 km in latitude) and 47 vertical levels (we use a finer vertical grid in the first 10 km, and the model top remains at 250 km).

The GCM simulations have been performed using an N_2 ice emissivity of 0.8 and an albedo between 0.67-0.74 (see Section 2.3). The surface N_2 pressure simulated in the model is constrained by these values and reaches 1-1.2 Pa in 2015 as observed by New Horizons. The albedo and emissivity of the bare ground (volatile-free surface) are set to 0.1 and 1 respectively, which corresponds to a terrain covered by dark red materials such as the informally named Cthulhu Macula. CH_4 ice emissivity is fixed at 0.8 in all simulations. The thermal conduction into the subsurface is performed with a low thermal inertia near the surface set to 20 J s$^{-1/2}$ m^{-2} K^{-1} to capture the short-period diurnal thermal waves and a larger thermal inertia below set to 800 J s$^{-1/2}$ m^{-2} K^{-1} to capture the much longer seasonal thermal waves that can penetrate deep into the high thermal inertia substrate. The rest of the settings are similar to those in Forget et al. [2017] and Bertrand and Forget [2017].

2.3. The set of simulations: 3 scenarios explored

The GCM simulations presented in this paper are derived from our most realistic VTM simulations, which best reproduce the threefold increase of surface pressure between 1988 and 2015 [Meza et al., 2019], with 1-1.2 Pa in 2015 [Stern et al., 2015]. We found three possible scenarios for the N_2 surface ice distribution:

- Scenario ♯1: No N_2 ice deposits outside Sputnik Planitia.
- Scenario ♯2: N_2 ice deposits in the low-elevated terrains of the northern mid-latitudes, as observed by New Horizons [Schmitt et al., 2017; Protopapa et al., 2017].
- Scenario ♯3: Same as Scenario ♯2 but with extra N_2 ice deposits in the non-observed southern hemisphere.

Figure 1 shows the initial (year 1984) surface ice distribution corresponding to these three scenarios as simulated in the GCM (the same distribution is obtained at the end of the GCM simulation in 2015 as it does not vary significantly within this time frame). Note that all scenarios have a N_2-free surface below 60°S. No VTM simulation was able to reproduce a realistic threefold increase of surface pressure while having N_2 ice deposits below 60°S during the 1988-2015 period. Such deposits would induced a strong condensation flow and trigger a surface pressure drop around year 2000 [Meza et al., 2019; Bertrand et al., 2019].

In this paper, we explore these scenarios with the new version of the LMD Pluto GCM, with a focus on Sputnik Planitia and the atmospheric circulation. Note that most of the previous GCM results shown in Forget et al. [2017] are still valid and are therefore not shown again (for instance, the steady state and the mixing of CH_4 and CO in the atmosphere, the homogeneous atmospheric temperatures, the ubiquity of katabatic winds).

3. Near surface winds in Sputnik Planitia

In this section, we present the near-surface circulation in Sputnik Planitia obtained in the high resolution GCM simulations for 2015 and compare the results with the available observations from New Horizons.

3.1. Model results: anti-clockwise flow and boundary currents

In all our GCM simulations, we obtain a near-surface anti-clockwise atmospheric current that flows over Sputnik Planitia, from its north-east to its south-west side, as shown by Figure 2.C and Figure 3. What triggers this current? The N_2 ice sheet is Pluto's heart, beating once every day as N_2 sublimes during daytime and condenses during nighttime. In 2015 (northern spring), Pluto's cardiac activity is relatively high as latitudes located above 38°N (Pluto's current arctic summer, Binzel et al. [2017]) experience constant insolation across a diurnal cycle, involving large N_2 sublimation rates [Forget et al., 2017]. Most of the sublimation occurs in the northern part of the ice sheet, under constant illumination, while most of the condensation occurs in the southern part, close to the winter polar night. This leads to a net sublimation flow of cold air from the northern to the southern part of the ice sheet. As the near-surface air flows from northern latitudes toward the equator, it is deflected westward by the Coriolis effect, like trade winds on the Earth and on Mars. This explains the dominant westward winds obtained in the northern part of Sputnik Planitia. Then, as it reaches the high relief western boundary of the basin (defined by mountain ranges that reach elevations of 5 km above the plains, Figure 2.A), the flow is deviated and follows the boundary down to the southern latitudes of the basin, such as terrestrial or Martian western boundary currents (WBC, Figure 4, Anderson [1976]; Joshi et al. [1994, 1995]). In the late afternoon, the flow reaches the south-eastern edge of Sputnik Planitia and is deviated back toward northern latitudes. The western boundary current is the main artery of the heart-shaped basin, as it transports significant amounts of air from one hemisphere to another (see Section 4.1.1).

We investigated further this anti-clockwise current by performing five new GCM simulations (not shown) similar to the reference case shown by Figure 2.C and Figure 3: (1) A simulation without N_2 condensation-sublimation produces a completely different circulation with south-to-north clockwise current characterized by much weaker winds (less than 1 m s^{-1}). (2) A simulation without the diurnal cycle (daily averaged insolation) produces an anti-clockwise circulation similar to the reference case. (3) A simulation without the high-relief south-eastern boundary of Sputnik Planitia (i.e. the basin extends to its south-east margin) produces the same circulation than the reference case but there is no northward return branch of the flow on the eastern regions (the winds are rushing into the extended south-east regions of the modified basin). (4) A simulation with a rotation period of 0 s (no Coriolis forcing) produces no westward deflection of the flow and thus no boundary current (the sublimation flow is oriented from north to south in the basin). (5) A simulation with a rotation period of 0.5 Earth days (instead of the real period of 6.387 Earth days) produces a stronger and narrower WBC (more confined to the western boundary of the basin) than that in the reference case, thus better resembling the WBC known on Earth and on Mars. The northward return branch of the flow in the eastern regions of Sputnik Planitia remains relatively unchanged.

These investigations further demonstrate that the WBC is forced by the N_2 condensation-sublimation flow and the deviation of the flow by the Coriolis force and the high-relief boundaries of Sputnik Planitia. This peculiar circulation compares well with the WBCs known on Mars and on Earth (they are dynamically equivalent in the sense that there is some degree of western intensification). However, note that on Pluto, the length scales are different since the WBC is confined in a 3-km deep, 1000-km wide basin. The examples of WBC on Mars and on Earth usually correspond to much larger areas, if not semi-infinite plans. One can estimate the length scale at which rotational effects become significant for meteorological phenomenons by calculating the Rossby radius of deformation R on Pluto, given by :

$$R = \frac{(gD)^{0.5}}{f_c} \tag{1}$$

Where g is the gravitational constant, D is the depth of the atmospheric layer, and f_c is the Coriolis parameter. Assuming $D = 3$ km (the depth of the basin where the near-surface flow is simulated), we obtain $R \sim 4000$ km. The Rossby radius of deformation is larger than the Sputnik Planitia basin, which explains why the WBC is not very narrow in the reference simulation. The WBC really emerges when we increase the rotation rate: in the simulation with a rotation period of 0.5 Earth days, the Rossby radius of deformation is decreased by a factor of almost 10 and becomes lower than the length scale of the basin.

3.2. Comparisons with possible indicators of aeolian activity on Pluto's surface

3.2.1. Wind streaks

New Horizons observations of Pluto revealed the presence of dark wind streaks located on the western side of Sputnik Planitia between 15°N-25°N [Stern et al., 2015], and oriented northwest-southeast (153±10°, Figure 2.B inset). As on Mars, the streaks form an elongated albedo contrast with the surrounding ice plains, slightly darkening the ice [Thomas et al., 1981; Greeley et al., 1993; Geissler, 2005]. Here they appear to stem from isolated water ice blocks, which here are sufficiently interior to Sputnik Planitia such that they may be floating on the N_2 ice. Modification of wind flow by these topographic obstacles is interpreted to be the cause of the surface albedo contrast [Stern et al., 2015]. Two separate wind streaks with different orientations sometimes stem from a single block, which could reflect recent circulation changes. The wind directions and the WBC predicted by the GCM are consistent with the wind directions derived from these streaks. Possible scenarios for the formation of the surface albedo contrast are discussed in the following section and in Section 5.1.

3.2.2. The westward extended dark plains

Sputnik Planitia displays relatively dark plains in its north (above 30°N) and western regions, which contrast with the brighter plains in its center, as shown by Figure 2.B. The difference of albedo between the dark and bright plains is ∼0.05 [Buratti et al., 2017]. The darker color correlates with a weaker spectral signature of N_2 and CH_4, interpreted as combination of a decrease of the size of the N_2-rich ice grains, but richer in CH_4, coexisting with a larger amount of CH_4-rich ice grains [Schmitt et al., 2017; Protopapa et al., 2017]. This probably reflects recent N_2 ice sublimation processes which could form, according to its binary phase diagram, CH_4-rich grains from the saturation of CH_4 diluted in the N_2-rich ice. This is supported by simulations performed with the Pluto VTM, showing that the latitudes north of 15°N experienced a net loss of N_2 ice during the 2000-2015 period [Bertrand et al., 2018], whereas latitudes south of 15°N experienced a net deposition. In 2015, the sublimation rate is especially high north of 38°N, which presently experiences constant illumination, explaining the much lower albedo of the plains located there. White et al. [2017] noted that the boundary between the dark and bright plains is located at 30°N, which corresponds to the Arctic Circle (the southernmost latitude that can experience continuous insolation over a diurnal period at least once during an orbit). They hypothesized that net sublimation north of 30°N is revealing and concentrating darker, older, dark material-infused ice that forms the bulk of the N_2 ice filling the Sputnik Planitia basin, while net condensation south of 30°N is depositing a thin veneer of fresh, bright N_2 ice onto the plains and onto the bright pitted uplands of east Tombaugh Regio (Figure 2.B). A similar process may be occurring at Triton's south pole, where sublimation of ices may be concentrating dark organic matter on the surface of the ice or exposing layers of this material which have built up in the ice over many seasonal cycles [Stansberry et al., 1989].

However, the band of dark plains extending south of 30°N down the western margin of Sputnik Planitia indicates that factors besides latitude-dependant insolation are also influential in defining the albedo contrast in the plains, and the observation of wind streaks here suggests that near-surface winds may play a role. Our GCM results are consistent with the hypothesis that eolian activity is uncovering dark plains in this western region of Sputnik Planitia, as the sublimation flow and the WBC obtained in our simulations produce windier conditions roughly above the dark plains, Figure 2.C. However, the exact mechanisms leading to an increase of sublimation or erosion at these dark plains remain uncertain. We discuss possible scenarios in Section 5.1.

4. General circulation regime on Pluto

In this section, we explore the general circulation regime obtained with the high resolution GCM simulations for 2015, for the three reference scenarios. We also present for the first time a low resolution GCM simulation performed over three entire Pluto years, and we describe the seasonal evolution of the circulation regime.

4.1. General circulation in 2015 from high resolution GCM runs

4.1.1. Meridional circulation

Figure 5 shows the zonally-averaged meridional mass stream functions and zonal winds obtained for 2015 in each GCM simulation. There are few differences between the three scenarios. In the lowermost atmospheric scale height (below 20 km altitude), the zonal mean meridional circulation is characterized by a flow from the northern to the southern latitudes, which is controlled by the sublimation-condensation flow of N_2 inside Sputnik Planitia and outside when mid-latitudinal N_2 deposits are present (scenarios ♯2 and ♯3). This is shown by the anti-clockwise circulation cells (left column on Figure 5), which remain open near the surface (there is no return branch) because of the net transport of N_2 from the summer hemisphere (sublimation) to the winter hemisphere (condensation). Most of this near-surface meridional flow is controlled by the WBC, described above, which only occurs in Sputnik Planitia. This current efficiently forces N-S meridional transport of N_2 within the first scale height (which is eventually strengthened by the presence of mid-latitude N_2 deposits).

Above 20 km, the zonal mean meridional circulation is also dominated by an anti-clockwise circulation in some cases, centered above the subsolar point and controlled by thermal gradients in the atmosphere. This thermal cell is not present in all three simulation cases. Note that the meridional circulation in the upper atmosphere remains weak at all longitudes, with winds lower than 1 m s^{-1}. If the zonally averaged meridional circulation is dominated by a southward flow, this is not true at all all longitudes and altitudes. Figure 6 shows the meridional air mass flow averaged between 45°S-45°N for different ranges of altitudes. In the lowest 5 km of the atmosphere (blue curves), most of the cross-equatorial transport of air occurs around longitude 180°, that is in Sputnik Planitia. The basin is an efficient channel to transport freshly-sublimed air, gaseous methane and other atmospheric constituents from one hemisphere to the other (in 2015 the transport is mostly from north to south). The two peaks at longitude $\sim$170° and $\sim$190° correspond to the southward flow and northward flow respectively associated with the western boundary current and the northward return branch of the flow, as shown on Figure 3.

In simulation ♯1, the cross-equatorial transport of air is mostly directed southward below 20 km but is balanced by northward currents above 20 km, at longitudes $\sim$120° and $\sim$330°. In simulation ♯3, the presence of mid-latitudinal deposits reinforces the sublimation-condensation flow and the cross-equatorial transport of air is mainly southward transport (in particular, the condensation at southern latitudes prevent northward return flow of air). This result can be compared with pre-New Horizons GCM predictions published by Toigo et al. [2015], which assumed that N_2 ice was covering both poles. This is also seen on Figure 5, showing small clockwise cells at high northern and southern latitudes in simulation ♯1. When mid-latitude N_2 ice deposits are present (Scenarios ♯2 and ♯3), the N-S meridional flux is strengthened and does not allow the formation of the clockwise cells.

4.1.2. Zonal circulation

The zonally averaged meridional flux is weak but is still sufficient to trigger westward winds at all latitudes, by conservation of angular momentum as the N_2 molecules are transported from one hemisphere to the other and move away from the rotation axis as they cross the equator (as shown by the red cells on Figure 5). Thus, we find that the general circulation of Pluto's atmosphere is dominated by a retro-rotation, with zonal westward winds reaching 8-13 m s^{-1} at altitudes 20-250 km. The wind amplitude decreases toward the poles, but the winds remain directed westward (e.g. 4 m s^{-1} westward winds are obtained at the mid-latitudes between 50 and 200 km altitude). This result is independent of the presence of mid-latitudinal N_2 ice deposits outside Sputnik Planitia, which do not significantly change the circulation regime. In fact, they provide an extra source of sublimated N_2 in the northern hemisphere and an extra condensation sink of N_2 in the southern hemisphere and therefore strengthen the cross equatorial transport of N_2 and the westward winds.

In Forget et al. [2017], Pluto's general circulation was shown to be extremely sensitive to the surface distribution of N_2 ice. In this paper, we show that it is not the case if we assume that N_2 ice fills Sputnik Planitia and eventually the mid-latitudes but not the poles. The critical new factor in the GCM is the better representation of the Sputnik Planitia basin, which is more extended toward southern latitudes than was assumed before. In the simulations performed by Forget et al. [2017], the basin was modeled by a circular crater located between 0°N and 45°N, while in reality, it extends southward down to 25°S. In our new GCM simulations, presented in this paper, there is therefore an unavoidable cross-equatorial transport of N_2 from its northern (sublimation-dominated) to its southern (condensation-dominated) part, which is sufficient to trigger westward winds in the upper atmosphere by conservation of angular momentum. Note that if we place a N_2 ice deposit at the south pole in 2015, then we obtain a prograde jet around the south pole, with eastward winds up to 5 m s^{-1}, while the retro-rotation remains dominant at other latitudes (Figure not shown). If the condensation flow toward the south pole is very strong, then momentum can be transferred from the pole to the equator through wave instability mechanisms, and trigger a super-rotation in Pluto's atmosphere, as shown in Fig.10b of Forget et al. [2017].

However, a scenario with N_2 condensation at the south pole is unrealistic for 2015. Surface pressure is currently increasing on Pluto, which suggests limited N_2 condensation in the southern winter hemisphere. In fact, if N_2 ice was covering the south pole, then the peak of surface pressure should have occurred around year 2000, according to the models [Bertrand et al., 2018, 2019; Meza et al., 2019]. The absence of N_2 ice deposits at the south pole during the 1988-2015 period (early northern spring) could be explained by a combination of (1) the high thermal inertia of the substrate, which would enable the south pole to store the heat accumulated during previous summer and release it during fall and winter, thus preventing N_2 condensation at the pole during this period [Bertrand et al., 2018], (2) the presence of high-elevated terrains at the south pole, and (3) a darker surface albedo at the south pole, induced by a long period of sublimation (previous southern summer) of the surface ices (N_2, CH_4) which would lead to the exposure of more dark red materials.

To conclude, the assumption that Pluto's general circulation is sensitive to the surface distribution of N_2 ice remains true, but our model strongly suggests a circulation regime dominated by a retro-rotation for 2015, assuming realistic distributions for N_2 ice. In addition, the WBC in Sputnik Planitia is present in all simulation cases. However, although the overall meridional flow pattern remains southward (in the zonal average) in all simulation cases, some variability in meridional transport is obtained, depending on the location of the N_2 ice reservoirs.

4.1.3. Thermal tides and waves

The solar-induced sublimation breathing from the surface N_2 ice deposits triggers atmospheric thermal tides that could explain the density fluctuations observed during stellar occultations of Pluto's atmosphere [Elliot et al., 2003; Person et al., 2008; Toigo et al., 2010; Forget et al., 2017]. In particular, the N_2 breathing in Sputnik Planitia is a strong and very localized perturbation of Pluto's atmosphere. As in Forget et al. [2017], we obtained thermal tides structures in the temperature profile of our high-resolution GCM simulations, shown by Figure 7. The properties of the thermal tides are very similar to the predictions presented in Forget et al. [2017] (with no south pole N_2 condensation), including (1) temperature variations of up to 0.1 K and 0.2 K for scenarios ♯1 and ♯3 respectively, (2) wavenumber = 1 tides with a 10-20 km vertical wavelength below 100 km and a longer wavelength above.

Signatures of other types of waves are also present in our GCM simulations. For instance, barotropic wave activity is seen, similar to that shown in Forget et al. [2017] in the case with south pole N_2 condensation, but with a much lower intensity. In addition, vertical motions are induced by the topography, in particular in the surroundings of Sputnik Planitia, and could lead to orographic gravity waves in the atmosphere. However, the horizontal, vertical, and time resolution of our simulations are not ideal to investigate and analyze these wave mechanisms in detail. Consequently, we reserve this study for a future work which will involve improved GCM simulations (e.g. with more constraints on N_2 ice surface distribution) and wave analysis tools.

4.2. Evolution of the circulation regime over an entire Pluto year

In this section, we explore how the general circulation of Pluto's atmosphere varies over the year, as seasonal N_2 deposits form or disappear in both hemispheres. We extended the GCM simulation at relatively low resolution (11.25° ×7.5°) from Earth year 1984 to year 2732, that is 3 entire Pluto years.

The initial state corresponds to Scenario ♯3, with mid-latitudinal bands of N_2 deposits. Here we focus only on the annual evolution of the atmospheric circulation. The detailed analysis of this multi-year Pluto simulation and associated sensitivity studies will be performed in a future work, mostly because more years are necessary to reach a perfectly balanced CH_4 cycle. Figures 8 and 9 show the zonal mean zonal winds obtained at 20 and 100 km respectively, whereas the bottom panel of Figure 8 shows the 3-year evolution of the zonal mean distribution of N_2 ice. In this simulation, there is few seasonal N_2 ice deposits at the poles, and the pressure cycle is similar to the cycles obtained in previous works [Bertrand and Forget, 2016; Bertrand et al., 2018, 2019]. We note that although the simulation is close to steady state, the results from the first year are slightly different from those from the second and third year. Consequently, we consider the first year as spin up time and we only analyze the third year.

We find that the retro-rotation at 20 km is maintained during most of Pluto's year, with a maximum westward wind of ~10-12 m s^{-1} centered above Sputnik Planitia. This is because there is always enough cross-equatorial transport of gaseous N_2 in Sputnik Planitia (and outside), from north to south in northern spring and summer or south to north during the opposite season. Around L_s=270-300° (southern summer), the zonal winds at this altitude are still directed westward but are significantly weaker. This is due to the larger extent of the ice sheet in the northern, compared to the southern, hemisphere (Sputnik Planitia is not symmetrical about the equator). Because of this asymmetry, the sources of N_2 are weaker than the sinks of N_2 during L_s=270-300°, and significant meridional transport during this period occurs in the northern part of the ice sheet, as shown by Figure 10. In other words, the cross-equatorial transport of gaseous N_2 from the southern to the northern part of the ice sheet is much weaker during this season, hence the weaker winds. Note that if large amounts of N_2 are still covering the southern summer hemisphere during this period, the retro-rotation would be strengthened. Interestingly, the retro-rotation is currently at its highest intensity, because the subsolar point is at ~50°N and there is preferential sublimation of N_2 from the mid-latitudinal deposits and from the northern part of Sputnik Planitia. Another maximum is obtained around year 2150 (Solar longitude L_s=218°) when the subsolar point is above the latitude ~33°S and the southern N_2 deposits are preferentially sublimating.

Figure 9 shows similar results at 100 km altitude. The retro-rotation in the upper atmosphere is maintained during most of Pluto's year. Note that the strongest winds are centered above Sputnik Planitia, and that the weaker winds are obtained at the equinoxes. A stronger prograde jet is obtained in the north hemisphere at 40°N during northern winter (L_s=270-315°). Figure 11 shows the zonal mean zonal winds obtained during this period. The prograde jet in the upper atmosphere results from the intense poleward N_2 condensation flow and the conservation of angular momentum. The figure also shows that the circulation can quickly switch from retrograde to prograde over a Pluto year.

5. Discussions

Despite different N_2 ice distribution, the three reference GCM simulations of this paper are characterized by the same circulation regime in 2015, that is an anti-clockwise current in Sputnik Planitia and a retro-rotation with ∼10 m s^{-1} westward winds in the upper atmosphere. In this section, we explore the possible impact of this circulation on Pluto's surface and geology.

5.1. Possible eolian processes impacting the surface ice

5.1.1. Effect of downward sensible heat flux

In this section, we evaluate the sensible heat flux above Sputnik Planitia (controlled by the temperature gradient and the near-surface atmospheric motions) and how it affects the N_2 ice albedo and composition. In the GCM, the sensible heat flux is calculated using the bulk aerodynamic formula:

$$H_s = \rho C_p C_d V_1 (T_s - T_{z1}), \tag{2}$$

where (T_s-T_{z1}) is the temperature difference between surface and atmosphere at altitude z_1 above the surface (in the model, the first atmospheric layer is at z_1=5 m), $C_d = [0.4/ln(z_1/z_0)]^2$ is the von Karman drag coefficient depending on the surface roughness z_0 (assumed to be 1 cm everywhere), ρ is the near surface air density ($\sim 10^{-4}$ kg m^{-3} in 2015), C_p is the atmospheric specific heat capacity (1000 J kg^{-1} K^{-1}) and V_1 is the horizontal wind speed at altitude z_1. Above Sputnik Planitia, the sensible heat flux transferred to the surface would be consumed through the latent heat of sublimation of N_2 ice and the maintenance of vapor pressure equilibrium. This can be approximated by:

$$H_s = L\frac{dM}{dt}, \tag{3}$$

where L is the latent heat of sublimation of N_2 ice (2.5×10^5 J Kg^{-1}), M is the mass of N_2 ice and t is time. According to the model, N_2 sublimation injects cold air into the atmosphere above Sputnik Planitia, leading to a weak thermal gradient $T_s - T_1$ and therefore a negligible surface heat flux during daytime. However, during nighttime, katabatic winds transport the near-surface air from the surrounding terrains towards Sputnik Planitia, filling the basin with an air warmer (43-46 K at 5 m) than the surface, which remains at the equilibrium temperature ($\sim$37 K). This thermal gradient leads to a downward sensible heat flux that warms the surface and limits nighttime N_2 condensation.

Assuming $\mid T_s - T_1 \mid = 9$ K and $V_1 = 3$ m s^{-1}, we find that the downward sensible heat flux in Sputnik Planitia can reach 11 mW m^{-2} during nighttime, which is significant since the radiative flux $\epsilon\ \sigma\ T^4$ is only 85 mW m^{-2} (when T = 37 K and $\epsilon = 0.8$). Hence the mass of N_2 condensing at night in Sputnik Planitia is significantly impacted by the sensible heat flux. This quantitative energy balance calculation shows, to first order, that the sensible heat flux cannot be systematically neglected in the surface energy budget despite the low density of the Plutonian atmosphere.

Our simulations show an enhancement of nighttime downward sensible heat flux along the northern and western boundary of Sputnik Planitia (Figure 12.A-B), because winds are stronger there (following the western boundary current and the anti-clockwise near-surface circulation) and because warmer air is injected at night from the surrounding dark material-covered slopes and terrains. This correlates to the darker plains of Sputnik Planitia and could play a role in changing the sublimation rates in these regions. In fact, there seems to be a pattern whereby the darkest plains in the mid-western part of Sputnik Planitia tend to be proximal to tall mountains, which could be explained by the larger sensible heat flux, induced by the downslope transport of warmer air from the top of these mountains to the plains by stronger katabatic winds.

In general, the model predicts that the near surface air injected at night into the western side of Sputnik Planitia remains $\sim$ 3 K warmer than the air injected into the center of the ice sheet. Combined with stronger winds due to the WBC, we find that the western terrains of the ice sheet could have lost, in 2015, about 10% more N_2 ice than the central terrains (about 3 mm). This mechanism could have occurred continuously over the last 15 years, as the N_2 ice condensation-sublimation rates and the near-surface circulation remained relatively unchanged during this period, according to the model [Bertrand et al., 2018]. In this case, the difference in ice loss between the western and central plains would reach $\sim$45 mm. Consequently, the action of downward sensible heat flux seems to be a possible process to explain the increase in N_2 sublimation in the western regions of Sputnik Planitia, as inferred from New Horizons observations. This process could induce a decrease in surface albedo which would lead to an amplifying positive feedback by increasing the absorption of incoming radiation and thus the sublimation rate (see Section 5.1.6).

5.1.2. Effect of mechanical erosion

Enhanced sublimation or mechanical erosion of N_2 ice by the winds over the ice sheet could help disrupt the ice, as has been suggested for the polar caps of CO_2 on Mars [Appéré et al., 2011; Spiga et al., 2011]. Our model results could support this idea, since the WBC induces stronger winds and therefore higher near-surface stress above the dark plains of Sputnik Planitia (Figure 12.C). However, because of Pluto's low surface pressure, the surface stress obtained with the GCM in these regions is of the order of μN m^{-2}, which is very low (100-1000 times weaker than on Mars). This does not appear to be enough to significantly darken the ice by erosion of N_2 ice and subsequent accumulation of dark materials, even if such a surface stress occurred continuously over the last 15 Earth years. Note that the erosion of N_2 ice could have helped forming a CH_4-rich layer on top of the surface and impact the spectrum of the surface, but it would also probably lead to a brighter surface as small CH_4 ice grains form above large transparent N_2 ice grains.

5.1.3. Effect of surface accumulation of haze particles

In this section we investigate how N_2 ice reservoirs impact the accumulation of haze particles onto Pluto's surface, and we examine the accumulation of haze particles in Sputnik Planitia as a process that is potentially responsible for the observed contrasts of color and composition on the surface of the ice sheet.

We have run the GCM with the haze parameterization described in Bertrand and Forget [2017], which reproduces to first order the photolysis of CH_4 molecules in the upper atmosphere by Lyman-α UV radiation, the production of gaseous haze precursors, and their conversion into solid particles (using a simple conversion scheme with a characteristic time for aerosol growth set to 10^7 s). In the model, the haze particles are passive tracers with a fixed uniform radius that only affects their sedimentation velocity. Although this parameterization is relatively simplified and not well validated, it remains reasonable to use it here to investigate the transport of haze particles by the circulation. As shown in Bertrand and Forget [2017], haze production in the upper atmosphere above the north pole in 2015 is more abundant than that at lower latitudes (because of constant illumination and thus constant CH_4 photolysis), and the modeled haze is more extensive in the northern hemisphere because the meridional circulation (and therefore the southward transport of haze particles) is relatively weak.

Figure 13 shows a global map of net surface haze accumulation as obtained with the low-resolution GCM simulation (Scenario ♯2) over the period 1984-2015, assuming 10 nm haze particles. The distribution of haze particles settling onto the surface is significantly impacted by N_2 condensation and sublimation flows. This is especially true for particles with a small sedimentation radius, such as 10 nm particles, which have a low sedimentation velocity (e.g. 4.6×10^{-4} m s^{-1} at 1 Pa near the surface).

The simulation shows that these particles are repelled from the surface of the plains by N_2 sublimation flows and drawn towards the surface by N_2 condensation flows and the katabatic winds [see Fig. 12 in Bertrand and Forget, 2017]. Whereas N_2 ice reservoirs located in the polar night continuously attract haze particles as well as N_2, those located in the polar day continuously repel haze particles. In the diurnal zone, daytime sublimation and nighttime condensation occur, but the condensation is much more efficient at attracting haze particles than sublimation is at repelling them. This is because N_2 ice is locally distributed in depressions [Bertrand and Forget, 2016], with katabatic winds on the surrounding slopes balancing daytime-induced sublimation flows and strengthening nighttime-induced condensation flows.

Consequently, according to the model, significant accumulation of haze particles could have occurred in low-latitude N_2 ice reservoirs over the period 1984-2015. The model predicts less accumulation in the reservoirs north of 38°N, which experienced constant illumination in 2015. In particular, the model suggests that the accumulation of haze particles could be up to 10 times larger in depressions containing N_2 ice than elsewhere. The haze accumulation predicted by the model is even larger in the southern regions of Sputnik Planitia, where the strong katabatic winds and intense condensation flows occurred during the 1984-2015 period. Note that Grundy et al. [2018] estimated that atmospheric haze particles compose 1.4% of Sputnik Planitia's present-day bulk, by assuming a uniform haze deposition rate across Pluto's surface. Here our modeling results suggest a larger fraction by a factor of up to 10 within the low-latitude N_2 ice reservoirs.

Figure 13 also shows larger haze accumulation in the north-western regions of Sputnik Planitia than in the north-eastern regions, by a factor of 3 in the plains and 6 on the outermost edges, according to the model. This is consistent with Schmitt et al. [Fig. 35 in 2017], which shows an increasing amount of red material in the north-western regions of Sputnik Planitia. Interestingly, in this figure the pattern of distribution of the red material is very similar to the wind pattern at its strongest during Pluto year, around $L_s = 225°$, in Figure 10. At this period very strong N-E winds blow from Cthulhu Macula and may lift and transport haze particle accumulated at the surface of this region (still highly mobile, as not included in ice) and deposit them at the surface of the N-W part of Sputnik Planitia.

In our simulation, the difference in ice contamination by haze particles across Sputnik Plantia is significant and could potentially be sufficient to impact the surface albedo by a few percents (and thus the sublimation-condensation rates) and lead to the observed contrasts of color and composition in Sputnik Planitia. This increased amount of impurities could also impact the ice rheology. Here the haze accumulation is mostly driven by the condensation flow, the strong katabatic winds in the western regions and by the near-surface circulation within Sputnik Planitia, although the low horizontal resolution of the global simulation may be too coarse here to properly represent the near-surface circulation.

Figure 12.D shows the net accumulation of haze particles in Sputnik Planitia over one Pluto day in 2015, modeled using the high-resolution GCM simulation. In 2015, the intense N_2 sublimation flow and the WBC north of Sputnik Planitia tend to repel the haze particles during daytime. However, at night, the condensation flows coupled to katabatic winds are efficient to put large amounts of particles onto the N_2 ice plains surrounding the Al-Idrisi, Zheng He, Barè and Hillary Montes. The haze accumulation patterns on Figure 12.D can be compared to the observations of dark plains in these regions, although we note that there are still expanses of bright plains here and that the boundaries between bright and dark plains tend to be more abrupt than what the simulation produces. We also note that haze accumulation is predicted in the eastern regions by the model, which is not supported by the observations showing that the plains of these regions remain bright.

In the southern regions of Sputnik Planitia, the haze particles could probably be quickly buried by the diurnal accumulation of N_2 ice, allowing the plains of these regions to remain bright. Our simulated haze deposition rates are stronger inside southern Sputnik Planitia than outside but remain of the order of 10^{-8}-10^{-7} kg m^{-2} per Pluto day, that is much below the N_2 deposition rates, which are of the order of 10^{-1} kg m^{-2} per Pluto day at this latitude and season (100-200 μm, see Figure 16). The high N_2 deposition rates in southern Sputnik Planitia should be sufficient to mask the haze particles accumulating in this region and prevent discoloration of the ice, in agreement with the observed bright surface of the southernmost plains of the ice sheet. To conclude, the transport of haze particles by the circulation seems to be a possible mechanism to trigger ice composition and color contrasts across Sputnik Planitia, although it remains difficut to assess with the model and the simplified haze parameterization.

5.1.4. Dark materials ejected from the dark troughs of Sputnik Planitia

At the northern edge of Sputnik Planitia, dark convective cells boundaries seem to correspond to troughs filled with dark materials [White et al., 2017]. The very dark plains observed in this region seem to be located around these dark troughs. Are dark materials blown away from these troughs as N_2 sublimates, thus darkening Spunik Planitia? In order to test this hypothesis, we added in the model a source of dark material roughly at the location of the very dark plains (above 40°N in Sputnik Planitia). The material is injected into the atmosphere during daytime, and is proportional to the sublimation rate of N_2.

Figure 14 shows how this material is spread into the atmosphere and Figure 15 shows the net surface accumulation obtained after three days following the first injection. The material is transported by the WBC from the northern to the southern latitudes of Sputnik Planitia. A larger surface accumulation of the material is found in the western regions of Sputnik Planitia, in good agreement with the observed location of the dark plains. Consequently, If large amounts of materials can be mobilized in the northern edge of Sputnik Planitia (from the dark troughs) as N_2 ice sublimes, they could accumulate in the north-western regions of Sputnik Planitia and trigger an albedo contrast such as observed by New Horizons.

5.1.5. Transport of ice grains

Could the contrast of color and composition observed in Sputnik Planitia also be due to transport of ice grains by the near-surface winds and the WBC? For instance, sublimation of a transparent granular ice layer could raise N_2 ice particles aloft, which could then be transported by the near-surface winds. Such particles may not sublimate quickly due to adiabatic cooling in the boundary layer [Hinson et al., 2017]. Alternatively, CH_4 rich particles mixed with N_2 could also be raised aloft very easily by the N_2 sublimation flow. This process has been suggested for the formation of dunes west of Sputnik Planitia [Telfer et al., 2018]. However, the observed dunes, thought to be composed of CH_4-rich ice particles, seem to correspond to brighter areas on the ice sheets surface and therefore cannot explain the observation of bright N_2-rich or dark CH_4-rich surface. In addition, the size of the CH_4 ice grains in Sputnik Planitia seem to be of the order of 1 mm [see Fig. 4.B in Protopapa et al., 2017], which is too large to be transported by Plutos winds and saltation processes [Telfer et al., 2018]. Consequently, the transport of ice grains by the near-surface circulation seems unlikely to be related to the albedo contrast observed between the dark and bright plains of Sputnik Planitia.

5.1.6. Surface albedo feedback

Albedo and composition positive feedbacks could take place to further increase the sublimation rate of N_2 ice over the dark plains. For instance, the difference of sensible heat flux over bright and dark plains could have triggered an albedo difference, which then could have amplified with time. We can roughly estimate the sublimation rate of N_2 by neglecting the internal heat flux and the sensible heat flux from the atmosphere and write the daytime surface energy balance as:

$$\epsilon\sigma T^4 = (1 - A)F - L\frac{dM}{dt}, \tag{4}$$

where F is the incoming solar flux (1 W m^{-2}), A is the N_2 surface albedo, T is the surface temperature (∼37 K), ϵ is the ice emissivity (∼0.8) and σ is the Stefan-Boltzmann constant. By assuming a N_2 ice albedo of 0.7 for the bright plains and 0.65 for the dark plains, we find differences in sublimation rate of 20%. By assuming albedos of 0.9 and 0.85, the difference increases up to a factor 4. This would correspond to a difference of sublimated thickness of N_2 ice of 30-60 μm over one Pluto day and 25-50 mm over the last 15 Earth years. Figure 16 shows the net budget of N_2 ice obtained over one Pluto day in 2015 in the reference case using an uniform albedo for N_2 ice and in the case of a lower albedo in the northern and western regions of Sputnik Planitia. Between 5°N-25°N, the slightly lower albedo of N_2 ice in the western regions of Sputnik Planitia is enough to invert the net surface energy balance and lead to a net diurnal loss of N_2 ice in these regions, whereas the bright central and eastern regions remain dominated by a net accumulation of N_2 ice.

To conclude, a strong contrast in sensible heat flux at night and the transport of dark material from a source located in the northern plains (and eventually erosion, haze deposition, ice grains transport, or another mechanism not mentioned in this paper) could have triggered an albedo contrast between the north-western and central plains of Sputnik Planitia. The cumulative effects of these mechanisms and the increased sunlight absorption by the darker surface seems to be sufficient to keep the energy balance positive and the surface sublimating in the western regions. This would allow further accumulation of dark material right at the surface, thus providing an additional positive albedo feedback to further limit any condensation in these regions.

5.1.7. Difference of ice thickness between the bright and dark plains

The plains of Sputnik Planitia are covered by polygonal cells, thought to be formed by convective motion of the ice within the ice sheet [McKinnon et al., 2016]. The edges of the cells appear to be depressed by few tens of meters relative to the centers. Around 30°N, the edges of the convective cells located within the dark plains remain relatively bright. This suggests a larger accumulation of N_2 ice along the depressions and valleys of the cells, with a resemblance to terrestrial snow subsisting during spring in the talwegs and valley paths. This accumulation could be triggered by winds or by less incoming insolation because of the topographic slopes.

Given the spatial extent (∼50 km) and homogeneity of these areas, it is reasonable to assume that the difference in N_2 ice sublimation underlying the origin of the color and composition contrasts involved an ice thickness of the order of at least a metre. In this paper, we have explored mechanisms involving the conductive heat flux from the atmosphere, the erosion of the ice induced by wind stress, the transport of ice grains, haze and dark material by near-surface winds and albedos positive feedbacks. The convective heat flux, the albedo positive feedback and the transport of dark material seem to be more efficient to trigger the observed contrasts between bright and dark plains. However, we estimate that they would involve a difference in sublimated ice thickness of the order of tens of millimeter over the last 15 years. Consequently, the observed contrast may have formed over longer timescales, involving these mechanisms over many plutonian years for instance.

5.2. Impact of the retro-rotation on the formation of the Bladed Terrain and Cthulhu Macula

A striking longitudinal asymmetry observed on Pluto by New Horizons is the presence of the CH_4-rich Bladed Terrain east of Sputnik Planitia, while the uplands of Cthulhu Macula to the southwest of the ice sheet are mostly volatile-free and covered by a thick mantle of dark red material, probably several meters thick. The atmospheric retro-rotation could play a role in the processes leading to this asymmetry. For instance, during periods of equatorial accumulation of CH_4 ice, the retro-rotation and the injection of cold N_2-rich air from Sputnik Planitia could transport and push gaseous CH_4 westward, so that it favors the accumulation of CH_4 ice at the westernmost longitudes (that is, east of Sputnik Planitia) leading to the formation of the Bladed Terrain there. A very small difference in accumulation between east (Cthulhu) and west (Tartarus Dorsa) longitudes could have been sufficient at first to trigger this asymmetry, because CH_4 ice accumulation in the west and haze accumulation darkening the surface of Cthulhu in the east would induce very efficient positive amplifying feedbacks strengthening these resurfacing processes [Earle et al., 2018]. As CH_4 ice accumulates, it would form large deposits at high altitude, leading another positive feedback between CH_4 condensation and altitude, assuming that CH_4 preferably condenses at high altitude in the equatorial regions (this is based on New Horizons observations, see Moore et al. [2018]). Of course, if the water ice bedrock already formed an asymmetry of altitude at the current location of Cthlhu and the Bladed Terrain, that may have been sufficient to accumulate CH_4 ice in the western hemisphere.

Another region of interest is the eastern part of Tombaugh Regio (the right lobe of the heart). Its surface is relatively bright and covered by N_2-rich and CH_4-rich frosts. Could it be a consequence of the retro-rotation of Pluto's atmosphere? The bright pitted uplands seen in the eastern part of Tombaugh Regio are thought to be a glacially-modified version of Bladed Terrain [Moore et al., 2018]. It is possible that they correspond to low-altitude Bladed Terrain deposits which became sufficiently bright at some point of Pluto's history to trigger N_2 ice condensation and accumulation on it, whereas high-altitude Bladed Terrain deposits remained N_2-free because located at much higher altitude. Then, N_2 ice remained in east Tombaugh Regio at it is very stable at these latitudes [Bertrand et al., 2018, 2019]. Alternatively, gaseous CH_4 subliming from the CH_4-rich Bladed Terrain would be transported westward by the retrograde winds and could quickly recondense in east Tombaugh Regio, thus forming bright ice deposits there. Albedo feedbacks would then be sufficient to trigger more CH_4 and N_2 condensation in this region [Bertrand et al., 2019; Earle et al., 2018]. However, we note that condensation of CH_4 west of the Bladed Terrain is not verified everywhere on Pluto. For instance, Bladed Terrain deposits are observed east of the Krun Macula region (south-east of Sputnik Planitia) but this region remains dark and is not covered by bright CH_4 frosts.

Finally, the ridges ("blades“) of the Bladed Terrain deposits display a dominant N-S orientation [Moore et al., 2018], which could also originate in part from this peculiar atmospheric circulation regime, although it may be a N-S-aligned sublimation texture due to equatorial location, as suggested by Moore et al. [2018]. In the future, we plan to further explore these ideas and investigate the processes leading to these longitudinal asymmetries and peculiar geological formations, by using high resolution long-term GCM simulations.

6. Conclusions

We explored Pluto's atmosphere dynamics by using an improved version of the 3D LMD Global Climate Model of Pluto's atmosphere, which now takes into account topographic datasets constructed for Pluto encounter hemisphere. We performed high resolution simulations of Pluto's climate for 2015, which are the result of 30-Earth-year simulations performed with the GCM at low resolution and 30-millions-year simulations performed with the 2D surface model (VTM). Based on the VTM results, we tested different possible scenarios in the GCM, assuming an initial distribution of N_2 ice only in the Sputnik Planitia basin or with additional mid-latitudinal N_2 ice deposits.

In all simulation cases, we obtain an intense near-surface circulation within Sputnik Planitia, totally controlled by the N_2 condensation-sublimation flow and the topography, and characterized in 2015 by an anti-clockwise spiral flow and a western boundary current. We explored if these near-surface winds could play a role in the formation of albedo and ice composition contrasts observed across Sputnik Planitia. We used the GCM to investigate different surface-atmosphere interactions involving the near-surface winds, such as the effect of the conductive heat flux from the atmosphere, the erosion of the ice, and the transport of ice grains and dark materials. We find that the cumulative effect of these mechanisms could trigger significant contrasts in ice sublimation rate and color, and could explain the formation of the bright and dark plains in Sputnik Planitia.

We also find that the near-surface circulation adds up to the thermal gradient in the atmosphere to trigger a zonally-averaged meridional transport of N_2 from the northern summer hemisphere to the southern winter hemisphere. By conservation of angular momentum, this leads unavoidably to a general circulation characterized by retrograde westward winds reaching up to 10 m s^{-1} above the equator, while meridional winds remain relatively weak at all longitudes (less than 1 m s^{-1}). This retro-rotation of Pluto's atmosphere is a unique circulation regime in the Solar system, except maybe on Triton, where pole-to-pole transport of N_2 could also lead to a similar regime. We find that the retro-rotation is maintained during most of Pluto's year. It could be responsible for many longitudinal asymmetries and geological features observed on Pluto's surface, such as the depletion of Bladed Terrains at eastern longitudes and the formation of bright pits in eastern Tombaugh regio, although this remains to be explored. Our work confirms that despite a frozen surface and a tenuous atmosphere, Pluto's climate is remarkably active.

Acknowledgments. We thank John Wilson, Bob Haberle and Melinda Kahre for insightful discussions and comparisons between Mars and Pluto. We thank the NASA New Horizons team for their excellent work on a fantastic mission and their interest in this research. We acknowledge the Centre National dEtudes Spatiales (CNES) for its financial support through its "Système Solaire" program. T. B. was supported for this research by an appointment to the National Aeronautics and Space Administration (NASA) Post-doctoral Program at the Ames Research Center administered by Universities Space

Research Association (USRA) through a contract with NASA. Electronic output from all model simulations will be made available to the public through the NASA Advanced Supercomputing (NAS) data portal (https://data.nas.nasa.gov/), which is housed at NASA Ames Research Center.

References

D. L. T. Anderson. The Low-Level Jet as a Western Boundary Current. *Monthly Weather Review*, 104:907, 1976. doi: 10.1175/1520-0493(1976)104⟨0907:TLLJAA⟩2.0.CO;2.

T. Appéré, B. Schmitt, Y. Langevin, S. Douté, A. Pommerol, F. Forget, A. Spiga, B. Gondet, and J.-P. Bibring. Winter and spring evolution of northern seasonal deposits on Mars from OMEGA on Mars Express. *Journal of Geophysical Research (Planets)*, 116:E05001, May 2011. doi: 10.1029/2010JE003762.

T. Bertrand and F. Forget. Observed glacier and volatile distribution on Pluto from atmo-spheretopography processes. *Nature*, 987, December 2016. doi: 10.1038/nature19337.

T. Bertrand and F. Forget. 3D modeling of organic haze in Pluto's atmosphere. *Icarus*, 287:72–86, May 2017. doi: 10.1016/j.icarus.2017.01.016.

T. Bertrand, F. Forget, O. M. Umurhan, W. M. Grundy, B. Schmitt, S. Protopapa, A. M. Zangari, O. L. White, P. M. Schenk, K. N. Singer, A. Stern, H. A. Weaver, L. A. Young, K. Ennico, and C. B. Olkin. The nitrogen cycles on Pluto over seasonal and astronomical timescales. *Icarus*, 309:277–296, July 2018. doi: 10.1016/j.icarus.2018.03.012.

T. Bertrand, F. Forget, O. M. Umurhan, J. M. Moore, L. A. Young, S. Protopapa, W. M. Grundy, B. Schmitt, R. D. Dhingra, and R. P. Binzel. The CH_4 cycles on Pluto over seasonal and astronomical timescales. *Icarus*, 329:148–165, Sep 2019. doi: 10.1016/j.icarus.2019.02.007.

R. P. Binzel, A. M. Earle, M. W. Buie, L. A. Young, S. A. Stern, C. B. Olkin, K. Ennico, J. M. Moore, W. Grundy, H. A. Weaver, C. M. Lisse, and T. R. Lauer. Climate zones on Pluto and Charon. *Icarus*, 287:30–36, May 2017. doi: 10.1016/j.icarus.2016.07.023.

B. J. Buratti, J. D. Hofgartner, M. D. Hicks, H. A. Weaver, S. A. Stern, T. Momary, J. A. Mosher, R. A. Beyer, A. J. Verbiscer, A. M. Zangari, L. A. Young, C. M. Lisse, K. Singer, A. Cheng, W. Grundy, K. Ennico, and C. B. Olkin. Global albedos of Pluto and Charon from LORRI New Horizons observations. *Icarus*, 287:207–217, May 2017. doi: 10.1016/j.icarus.2016.11.012.

A. M. Earle, R. P. Binzel, L. A. Young, S. A. Stern, K. Ennico, W. Grundy, C. B. Olkin, H. A. Weaver, and New Horizons Surface Composition Theme. Albedo matters: Understanding runaway albedo variations on Pluto. *Icarus*, 303:1–9, March 2018. doi: 10.1016/j.icarus.2017.12.015.

J. L. Elliot, A. Ates, B. A. Babcock, A. S. Bosh, M. W. Buie, K. B. Clancy, E. W. Dunham, S. S. Eikenberry, D. T. Hall, S. D. Kern, S. K. Leggett, S. E. Levine, D.-S. Moon, C. B. Olkin, D. J. Osip, J. M. Pasachoff, B. E. Penprase, M. J. Person, S. Qu, J. T. Rayner, L. C. Roberts, C. V. Salyk, S. P. Souza, R. C. Stone, B. W. Taylor, D. J. Tholen, J. E. Thomas-Osip, D. R. Ticehurst, and L. H. Wasserman. The recent expansion of Pluto's atmosphere. *Nature*, 424:165–168, July 2003. doi: 10.1038/nature01762.

F. Forget, T. Bertrand, M. Vangvichith, J. Leconte, E. Millour, and E. Lellouch. A post-new horizons global climate model of Pluto including the N_2, CH_4 and CO cycles. *Icarus*, 287:54–71, May 2017. doi: 10.1016/j.icarus.2016.11.038.

P. E. Geissler. Three decades of Martian surface changes. *Journal of Geophysical Research (Planets)*, 110:E02001, February 2005. doi: 10.1029/2004JE002345.

R. Greeley, A. Skypeck, and J. B. Pollack. Martian aeolian features and deposits - Comparisons with general circulation model results. *J. Geophys. Res.,* , 98:3183–3196, February 1993. doi: 10.1029/92JE02580.

W. M. Grundy, R. P. Binzel, B. J. Buratti, J. C. Cook, D. P. Cruikshank, C. M. Dalle Ore, A. M. Earle, K. Ennico, C. J. A. Howett, A. W. Lunsford, C. B. Olkin, A. H. Parker, S. Philippe, S. Protopapa, E. Quirico, D. C. Reuter, B. Schmitt, K. N. Singer, A. J. Verbiscer, R. A. Beyer, M. W. Buie, A. F. Cheng, D. E. Jennings, I. R. Linscott, J. W. Parker, P. M. Schenk, J. R. Spencer, J. A. Stansberry, S. A. Stern, H. B. Throop, C. C. C. Tsang, H. A. Weaver, G. E. Weigle, and L. A. Young. Surface compositions across Pluto and Charon. *Science*, 351:aad9189, March 2016. doi: 10.1126/science.aad9189.

W. M. Grundy, T. Bertrand, R. P. Binzel, M. W. Buie, B. J. Buratti, A. F. Cheng, J. C. Cook, D. P. Cruikshank, S. L. Devins, C. M. Dalle Ore, A. M. Earle, K. Ennico, F. Forget, P. Gao, G. R. Gladstone, C. J. A. Howett, D. E. Jennings, J. A. Kammer, T. R. Lauer, I. R. Linscott, C. M. Lisse, A. W. Lunsford, W. B. McKinnon, C. B. Olkin, A. H. Parker, S. Protopapa, E. Quirico, D. C. Reuter, B. Schmitt, K. N. Singer, J. A. Spencer, S. A. Stern, D. F. Strobel, M. E. Summers, H. A. Weaver, G. E. Weigle, M. L. Wong, E. F. Young, L. A. Young, and X. Zhang. Pluto's haze as a surface material. *Icarus*, 314:232–245, November 2018. doi: 10.1016/j.icarus.2018.05.019.

C. J. Hansen and D. A. Paige. Seasonal Nitrogen Cycles on Pluto. *Icarus*, 120:247–265, April 1996. doi: 10.1006/icar.1996.0049.

D. P. Hinson, I. R. Linscott, L. A. Young, G. L. Tyler, S. A. Stern, R. A. Beyer, M. K. Bird, K. Ennico, G. R. Gladstone, C. B. Olkin, M. Pätzold, P. M. Schenk, D. F. Strobel, M. E. Summers, H. A. Weaver, and W. W. Woods. Radio occultation measurements of Pluto's neutral atmosphere with New Horizons. *Icarus*, 290:96–111, July 2017. doi: 10.1016/j.icarus.2017.02.031.

A. D. Howard, J. M. Moore, O. M. Umurhan, O. L. White, R. S. Anderson, W. B. McKinnon, J. R. Spencer, P. M. Schenk, R. A. Beyer, S. A. Stern, K. Ennico, C. B. Olkin, H. A. Weaver, and L. A. Young. Present and past glaciation on Pluto. *Icarus*, 287:287–300, May 2017. doi: 10.1016/j.icarus.2016.07.006.

M. M. Joshi, S. R. Lewis, P. L. Read, and D. C. Catling. Western boundary currents in the atmosphere of Mars. *Nature*, 367:548–552, February 1994. doi: 10.1038/367548a0.

M. M. Joshi, S. R. Lewis, P. L. Read, and D. C. Catling. Western boundary currents in the Martian atmosphere: Numerical simulations and observational evidence. *J. Geophys. Res.,* , 100:5485–5500, March 1995. doi: 10.1029/94JE02716.

W. B. McKinnon, F. Nimmo, T. Wong, P. M. Schenk, O. L. White, J. H. Roberts, J. M. Moore, J. R. Spencer, A. D. Howard, O. M. Umurhan, S. A. Stern, H. A. Weaver, C. B. Olkin, L. A. Young, K. E. Smith, R. Beyer, M. Buie, B. Buratti, A. Cheng, D. Cruikshank, C. Dalle Ore, R. Gladstone, W. Grundy, T. Lauer, I. Linscott, J. Parker, S. Porter, H. Reitsema, D. Reuter, S. Robbins, M. Showalter, K. Singer, D. Strobel, M. Summers, L. Tyler, M. Banks, O. Barnouin, V. Bray, B. Carcich, A. Chaikin, C. Chavez, C. Conrad, D. Hamilton, C. Howett, J. Hofgartner, J. Kammer, C. Lisse, A. Marcotte, A. Parker, K. Retherford, M. Saina, K. Runyon, E. Schindhelm, J. Stansberry, A. Steffl, T. Stryk, H. Throop, C. Tsang, A. Verbiscer, H. Winters, A. Zangari, and G. a. I. T. T. New Horizons Geology. Convection in a volatile nitrogen-ice-rich layer drives Pluto's geological vigour. *Nature*, 534:82–85, June 2016. doi: 10.1038/nature18289.

E. Meza, B. Sicardy, M. Assafin, J. L. Ortiz, T. Bertrand, E. Lellouch, J. Desmars, F. Forget, D. Bérard, A. Doressoundiram, J. Lecacheux, J. Marques Oliveira, F. Roques,

T. Widemann, F. Colas, F. Vachier, S. Renner, R. Leiva, F. Braga-Ribas, G. Benedetti-Rossi, J. I. B. Camargo, A. Dias-Oliveira, B. Morgado, A. R. Gomes-Júnior, R. Vieira-Martins, R. Behrend, A. Castro Tirado, R. Duffard, N. Morales, P. Santos-Sanz, M. Jelínek, R. Cunniffe, R. Querel, M. Harnisch, R. Jansen, A. Pennell, S. Todd, V. D. Ivanov, C. Opitom, M. Gillon, E. Jehin, J. Manfroid, J. Pollock, D. E. Reichart, J. B. Haislip, K. M. Ivarsen, A. P. LaCluyze, A. Maury, R. Gil-Hutton, V. Dhillon, S. Littlefair, T. Marsh, C. Veillet, K. L. Bath, W. Beisker, H. J. Bode, M. Kretlow, D. Herald, D. Gault, S. Kerr, H. Pavlov, O. Faragó, O. Klös, E. Frappa, M. Lavayssière, A. A. Cole, A. B. Giles, J. G. Greenhill, K. M. Hill, M. W. Buie, C. B. Olkin, E. F. Young, L. A. Young, L. H. Wasserman, M. Devogèle, R. G. French, F. B. Bianco, F. Marchis, N. Brosch, S. Kaspi, D. Polishook, I. Manulis, M. Ait Moulay Larbi, Z. Benkhaldoun, A. Daassou, Y. El Azhari, Y. Moulane, J. Broughton, J. Milner, T. Dobosz, G. Bolt, B. Lade, A. Gilmore, P. Kilmartin, W. H. Allen, P. B. Graham, B. Loader, G. McKay, J. Talbot, S. Parker, L. Abe, Ph. Bendjoya, J. P. Rivet, D. Vernet, L. Di Fabrizio, V. Lorenzi, A. Magazzú, E. Molinari, K. Gazeas, L. Tzouganatos, A. Carbognani, G. Bonnoli, A. Marchini, G. Leto, R. Zanmar Sanchez, L. Mancini, B. Kattentidt, M. Dohrmann, K. Guhl, W. Rothe, K. Walzel, G. Wortmann, A. Eberle, D. Hampf, J. Ohlert, G. Krannich, G. Murawsky, B. Gährken, D. Gloistein, S. Alonso, A. Román, J. E. Communal, F. Jabet, S. deVisscher, J. Sérot, T. Janik, Z. Moravec, P. Machado, A. Selva, C. Perelló, J. Rovira, M. Conti, R. Papini, F. Salvaggio, A. Noschese, V. Tsamis, K. Tigani, P. Barroy, M. Irzyk, D. Neel, J. P. Godard, D. Lanoiselée, P. Sogorb, D. Vérilhac, M. Bretton, F. Signoret, F. Ciabattari, R. Naves, M. Boutet, J. De Queiroz, P. Lindner, K. Lindner, P. Enskonatus, G. Dangl, T. Tordai, H. Eichler, J. Hattenbach, C. Peterson, L. A. Molnar, and R. R. Howell. Lower atmosphere and pressure evolution on Pluto from ground-based stellar occultations, 1988-2016. *Astronomy and Astrophysics*, 625:A42, May 2019. doi: 10.1051/0004-6361/201834281.

J. M. Moore, A. D. Howard, O. M. Umurhan, O. L. White, P. M. Schenk, R. A. Beyer, W. B. McKinnon, J. R. Spencer, K. N. Singer, W. M. Grundy, A. M. Earle, B. Schmitt, S. Protopapa, F. Nimmo, D. P. Cruikshank, D. P. Hinson, L. A. Young, S. A. Stern, H. A. Weaver, C. B. Olkin, K. Ennico, G. Collins, T. Bertrand, F. Forget, F. Scipioni, and New Horizons Science Team. Bladed Terrain on Pluto: Possible origins and evolution. *Icarus*, 300:129–144, January 2018. doi: 10.1016/j.icarus.2017.08.031.

J. E. Moores, C. L. Smith, A. D. Toigo, and S. D. Guzewich. Penitentes as the origin of the bladed terrain of Tartarus Dorsa on Pluto. *Nature*, 541:188–190, January 2017. doi: 10.1038/nature20779.

C. B. Olkin, J. R. Spencer, W. M. Grundy, A. H. Parker, R. A. Beyer, P. M. Schenk, C. J. A. Howett, S. A. Stern, D. C. Reuter, H. A. Weaver, L. A. Young, K. Ennico, R. P. Binzel, M. W. Buie, J. C. Cook, D. P. Cruikshank, C. M. Dalle Ore, A. M. Earle, D. E. Jennings, K. N. Singer, I. E. Linscott, A. W. Lunsford, S. Protopapa, B. Schmitt, E. Weigle, and the New Horizons Science Team. The Global Color of Pluto from New Horizons. *Astron. J.,* , 154:258, December 2017. doi: 10.3847/1538-3881/aa965b.

M. J. Person, J. L. Elliot, A. A. S. Gulbis, C. A. Zuluaga, B. A. Babcock, A. J. McKay, J. M. Pasachoff, S. P. Souza, W. B. Hubbard, C. A. Kulesa, D. W. McCarthy, S. D. Benecchi, S. E. Levine, A. S. Bosh, E. V. Ryan, W. H. Ryan, A. Meyer, J. Wolf, and J. Hill. Waves in Pluto's Upper Atmosphere. *Astrophys. J.*, 136:1510–1518, October 2008. doi: 10.1088/0004-6256/136/4/1510.

S. Protopapa, W. M. Grundy, D. C. Reuter, D. P. Hamilton, C. M. Dalle Ore, J. C. Cook, D. P. Cruikshank, B. Schmitt, S. Philippe, E. Quirico, R. P. Binzel, A. M. Earle, K. Ennico, C. J. A. Howett, A. W. Lunsford, C. B. Olkin, A. Parker, K. N. Singer, A. Stern, A. J. Verbiscer, H. A. Weaver, and L. A. Young. Pluto's global surface composition through pixel-by-pixel Hapke modeling of New Horizons Ralph/LEISA data. *Icarus*, 287:218–228, May 2017. doi: 10.1016/j.icarus.2016.11.028.

P. M. Schenk, R. A. Beyer, W. B. McKinnon, J. M. Moore, J. R. Spencer, O. L. White, K. Singer, F. Nimmo, C. Thomason, T. R. Lauer, S. Robbins, O. M. Umurhan, W. M. Grundy, S. A. Stern, H. A. Weaver, L. A. Young, K. E. Smith, C. Olkin, New Horizons Geology, and Geophysics Investigation Team. Basins, fractures and volcanoes: Global cartography and topography of Pluto from New Horizons. *Icarus*, 314:400–433, November 2018. doi: 10.1016/j.icarus.2018.06.008.

B. Schmitt, S. Philippe, W. M. Grundy, D. C. Reuter, R. Cote, E. Quirico, S. Protopapa, L. A. Young, R. P. Binzel, J. C. Cook, D. P. Cruikshank, C. M. Dalle Ore, A. M. Earle, K. Ennico, C. J. A. Howett, D. E. Jennings, I. R. Linscott, A. W. Lunsford, C. B. Olkin, A. H. Parker, J. W. Parker, K. N. Singer, J. R. Spencer, J. A. Stansberry, S. A. Stern, C. C. C. Tsang, A. J. Verbiscer, and H. A. Weaver. Physical state and distribution of materials at the surface of Pluto from New Horizons LEISA imaging spectrometer. *Icarus*, 287:229–260, May 2017. doi: 10.1016/j.icarus.2016.12.025.

A. Spiga, F. Forget, J.-B. Madeleine, L. Montabone, S. R. Lewis, and E. Millour. The impact of martian mesoscale winds on surface temperature and on the determination of thermal inertia. *Icarus*, 212:504–519, April 2011. doi: 10.1016/j.icarus.2011.02.001.

J. A. Stansberry, J. I. Lunine, and M. G. Tomasko. Upper limits on possible photochemical hazes on Pluto. *Geophys. Res. Lett.*, 16:1221–1224, November 1989. doi: 10.1029/GL016i011p01221.

S. A. Stern, F. Bagenal, K. Ennico, G. R. Gladstone, W. M. Grundy, W. B. McKinnon, J. M. Moore, C. B. Olkin, J. R. Spencer, H. A. Weaver, L. A. Young, T. Andert, J. Andrews, M. Banks, B. Bauer, J. Bauman, O. S. Barnouin, P. Bedini, K. Beisser, R. A. Beyer, S. Bhaskaran, R. P. Binzel, E. Birath, M. Bird, D. J. Bogan, A. Bowman, V. J. Bray, M. Brozovic, C. Bryan, M. R. Buckley, M. W. Buie, B. J. Buratti, S. S. Bushman, A. Calloway, B. Carcich, A. F. Cheng, S. Conard, C. A. Conrad, J. C. Cook, D. P. Cruikshank, O. S. Custodio, C. M. Dalle Ore, C. Deboy, Z. J. B. Dischner, P. Dumont, A. M. Earle, H. A. Elliott, J. Ercol, C. M. Ernst, T. Finley, S. H. Flanigan, G. Fountain, M. J. Freeze, T. Greathouse, J. L. Green, Y. Guo, M. Hahn, D. P. Hamilton, S. A. Hamilton, J. Hanley, A. Harch, H. M. Hart, C. B. Hersman, A. Hill, M. E. Hill, D. P. Hinson, M. E. Holdridge, M. Horanyi, A. D. Howard, C. J. A. Howett, C. Jackman, R. A. Jacobson, D. E. Jennings, J. A. Kammer, H. K. Kang, D. E. Kaufmann, P. Kollmann, S. M. Krimigis, D. Kusnierkiewicz, T. R. Lauer, J. E. Lee, K. L. Lindstrom, I. R. Linscott, C. M. Lisse, A. W. Lunsford, V. A. Mallder, N. Martin, D. J. McComas, R. L. McNutt, D. Mehoke, T. Mehoke, E. D. Melin, M. Mutchler, D. Nelson, F. Nimmo, J. I. Nunez, A. Ocampo, W. M. Owen, M. Paetzold, B. Page, A. H. Parker, J. W. Parker, F. Pelletier, J. Peterson, N. Pinkine, M. Piquette, S. B. Porter, S. Protopapa, J. Redfern, H. J. Reitsema, D. C. Reuter, J. H. Roberts, S. J. Robbins, G. Rogers, D. Rose, K. Runyon, K. D. Retherford, M. G. Ryschkewitsch, P. Schenk, E. Schindhelm, B. Sepan, M. R. Showalter, K. N. Singer, M. Soluri, D. Stanbridge, A. J. Steffl,

D. F. Strobel, T. Stryk, M. E. Summers, J. R. Szalay, M. Tapley, A. Taylor, H. Taylor, H. B. Throop, C. C. C. Tsang, G. L. Tyler, O. M. Umurhan, A. J. Verbiscer, M. H. Versteeg, M. Vincent, R. Webbert, S. Weidner, G. E. Weigle, O. L. White, K. Whittenburg, B. G. Williams, K. Williams, S. Williams, W. W. Woods, A. M. Zangari, and E. Zirnstein. The Pluto system: Initial results from its exploration by New Horizons. *Science*, 350:aad1815, October 2015. doi: 10.1126/science.aad1815.

D. F. Strobel, X. Zhu, M. E. Summers, and M. H. Stevens. On the Vertical Thermal Structure of Pluto's Atmosphere. *Icarus*, 120:266–289, April 1996. doi: 10.1006/icar.1996.0050.

M. W. Telfer, E. J. R. Parteli, J. Radebaugh, R. A. Beyer, T. Bertrand, F. Forget, F. Nimmo, W. M. Grundy, J. M. Moore, S. A. Stern, J. Spencer, T. R. Lauer, A. M. Earle, R. P. Binzel, H. A. Weaver, C. B. Olkin, L. A. Young, K. Ennico, K. Runyon, and aff12. Dunes on Pluto. *Science*, 360:992–997, June 2018. doi: 10.1126/science.aao2975.

P. Thomas, J. Veverka, S. Lee, and A. Bloom. Classification of wind streaks on Mars. *Icarus*, 45:124–153, January 1981. doi: 10.1016/0019-1035(81)90010-5.

A. D. Toigo, P. J. Gierasch, B. Sicardy, and E. Lellouch. Thermal tides on Pluto. *Icarus*, 208:402–411, July 2010. doi: 10.1016/j.icarus.2010.01.027.

A. D. Toigo, R. G. French, P. J. Gierasch, S. D. Guzewich, X. Zhu, and M. I. Richardson. General circulation models of the dynamics of Pluto's volatile transport on the eve of the New Horizons encounter. *Icarus*, 254:306–323, July 2015. doi: 10.1016/j.icarus.2015.03.034.

O. L. White, J. M. Moore, W. B. McKinnon, J. R. Spencer, A. D. Howard, P. M. Schenk, R. A. Beyer, F. Nimmo, K. N. Singer, O. M. Umurhan, S. A. Stern, K. Ennico, C. B.

Olkin, H. A. Weaver, L. A. Young, A. F. Cheng, T. Bertrand, R. P. Binzel, A. M. Earle, W. M. Grundy, T. R. Lauer, S. Protopapa, S. J. Robbins, and B. Schmitt. Geological mapping of Sputnik Planitia on Pluto. *Icarus*, 287:261–286, May 2017. doi: 10.1016/j.icarus.2017.01.011.

L. A. Young. Pluto's Seasons: New Predictions for New Horizons. *Astrophys. J.l*, 766: L22, April 2013. doi: 10.1088/2041-8205/766/2/L22.

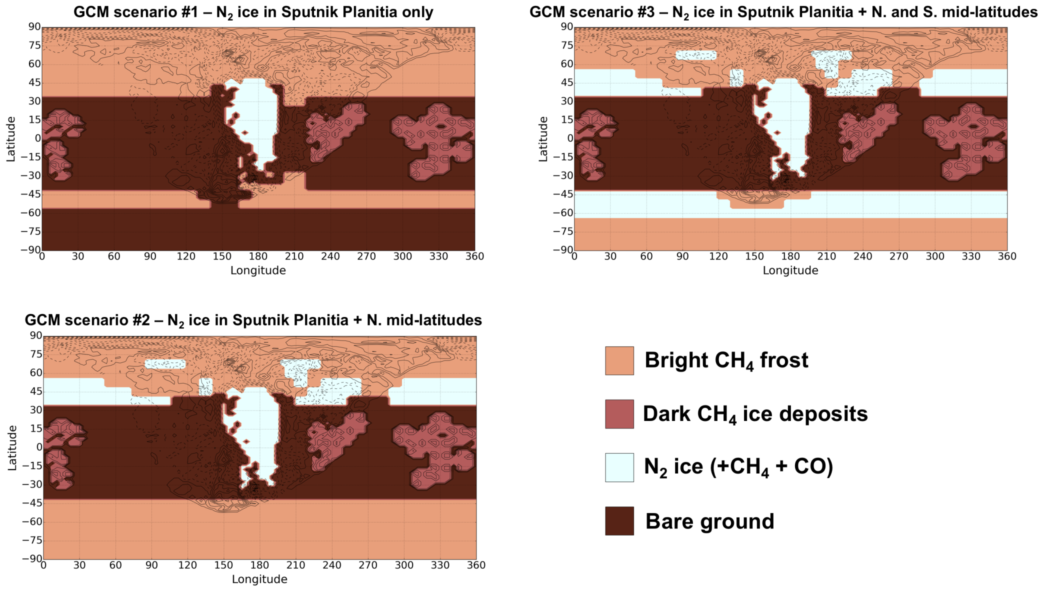

Figure 1. Map of initial surface ice distribution for the three GCM simulations. Albedos of each ice have been set so that the surface pressure and the atmospheric mixing ratio of CH_4 match the observations made by New Horizons in 2015. ♯1: A_{N2}=0.7,A_{CH4}=0.65. ♯2: A_{N2}=0.74,A_{CH4}=0.68. ♯3: A_{N2}=0.67,A_{CH4}=0.7.

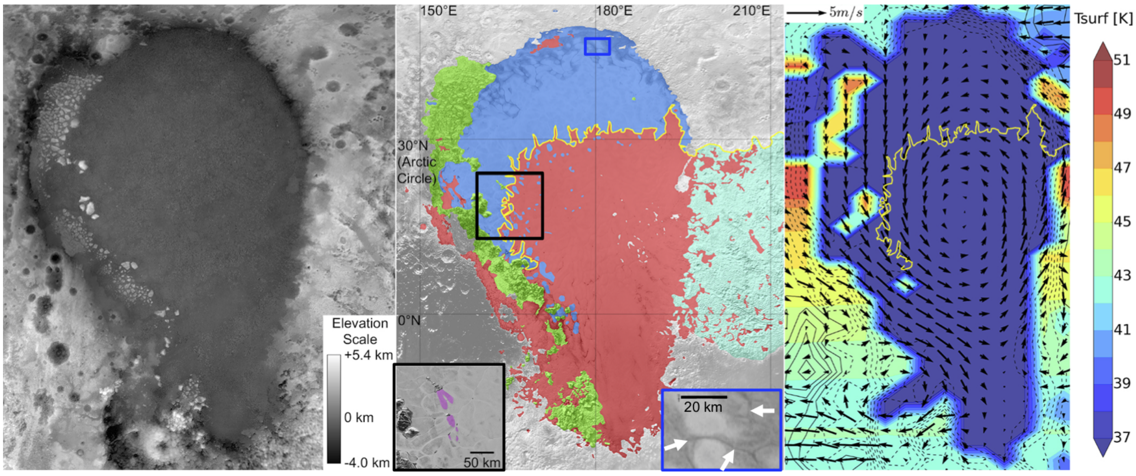

Figure 2. (A) Stereo digital elevation model (DEM) of Sputnik Planitia and surrounding terrain [Schenk et al., 2018]. (B) Simplified version of the geological map of White et al. [2017] depicting bright N_2 ice plains (red), dark N_2 ice plains (blue), mountains and hills lining the western rim of Sputnik Planitia (green), and bright pitted uplands of east Tombaugh Regio (cyan). Yellow line maps the continuous boundary between the bright and dark plains, as well as the northern boundary of the bright pitted uplands. Black box indicates the location of features in Sputnik Planitia interpreted as wind streaks, as mapped in purple in the inset (adapted from Stern et al. [2015]; Telfer et al. [2018]). Blue box and white arrows indicates the location of dark troughs, possibly filled with dark materials White et al. [2017]. (C) Map of diurnal mean horizontal winds in Sputnik Planitia obtained with the model for July 2015 at 1000 m above the surface. Yellow line replicates the bright/dark boundary in (B).

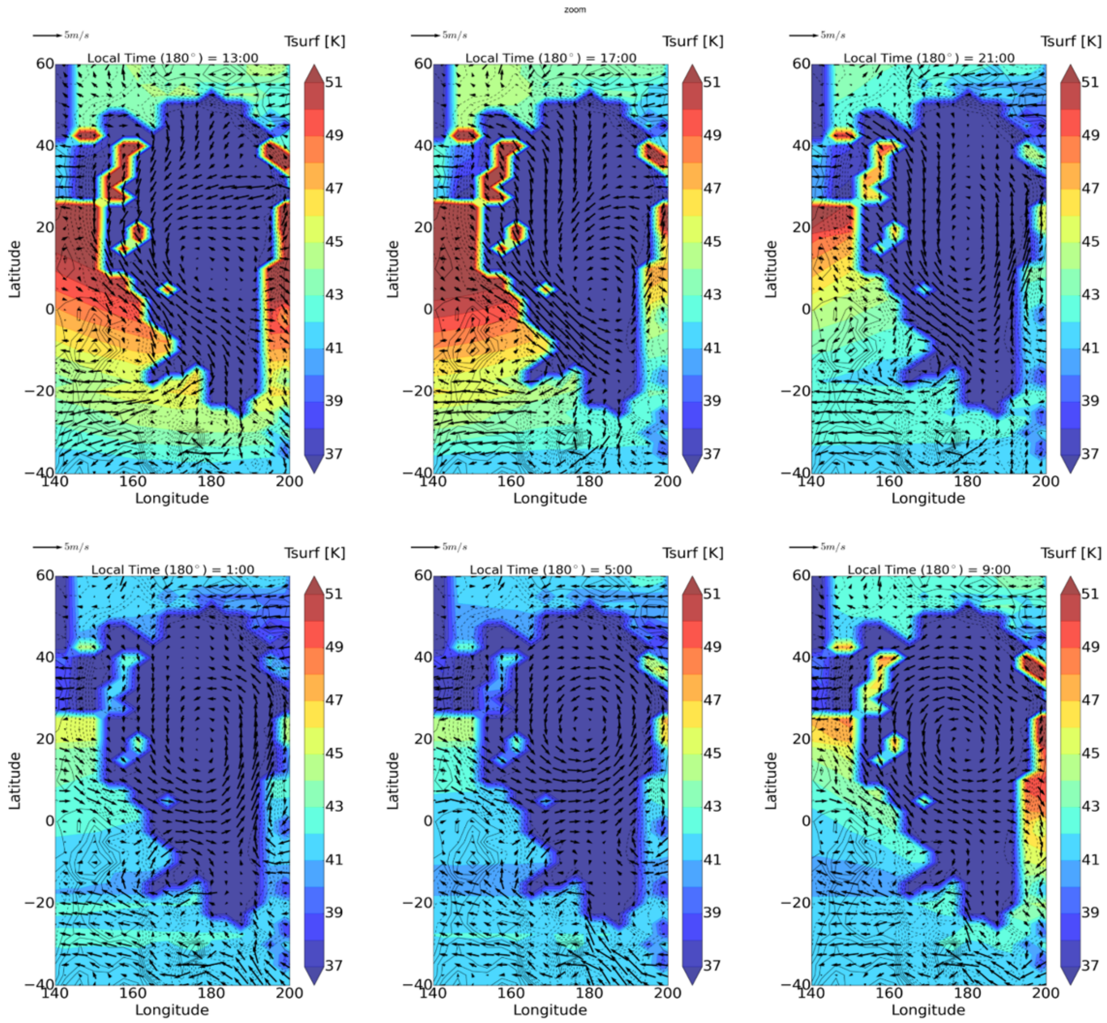

Figure 3. The beating of Pluto's heart: diurnal variations of horizontal winds in Sputnik Planitia obtained with the GCM for July 2015 at 1000 m above the surface (for Scenario ♯1), showing western and eastern boundary currents. Winds are strongest during afternoon and weakest during morning. The anti-clockwise atmospheric spiral circulates continuously. Similar results are obtained for Scenario ♯2 and ♯3 (not shown)

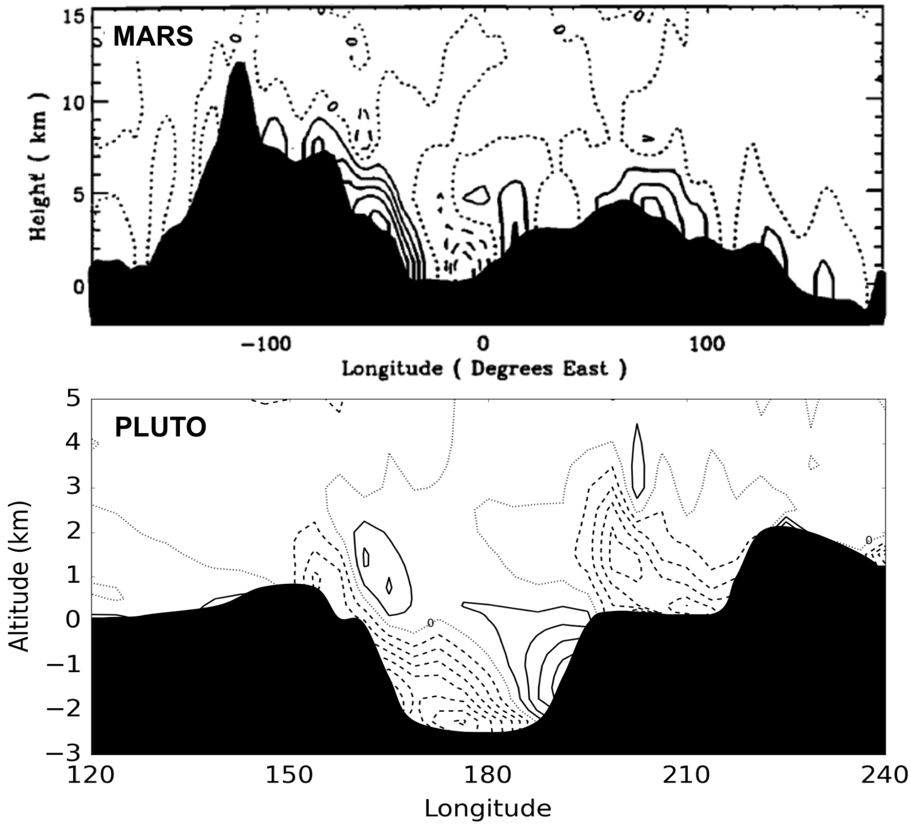

Figure 4. Cross-sections of the diurnal-averaged meridional wind (A) from Mars GCM simulations by Joshi et al. [1994], at the equator for northern summer solstice conditions (clockwise current) (B) from our Pluto GCM simulations, at the equator in the encounter hemisphere, in 2015 (northern spring, anti-clockwise current). The topographic profiles are shown in black. Contour intervals are 5 m s^{-1} for Mars and 0.4 m s^{-1} for Pluto, with the zero-contour dotted and negative contours dashed.

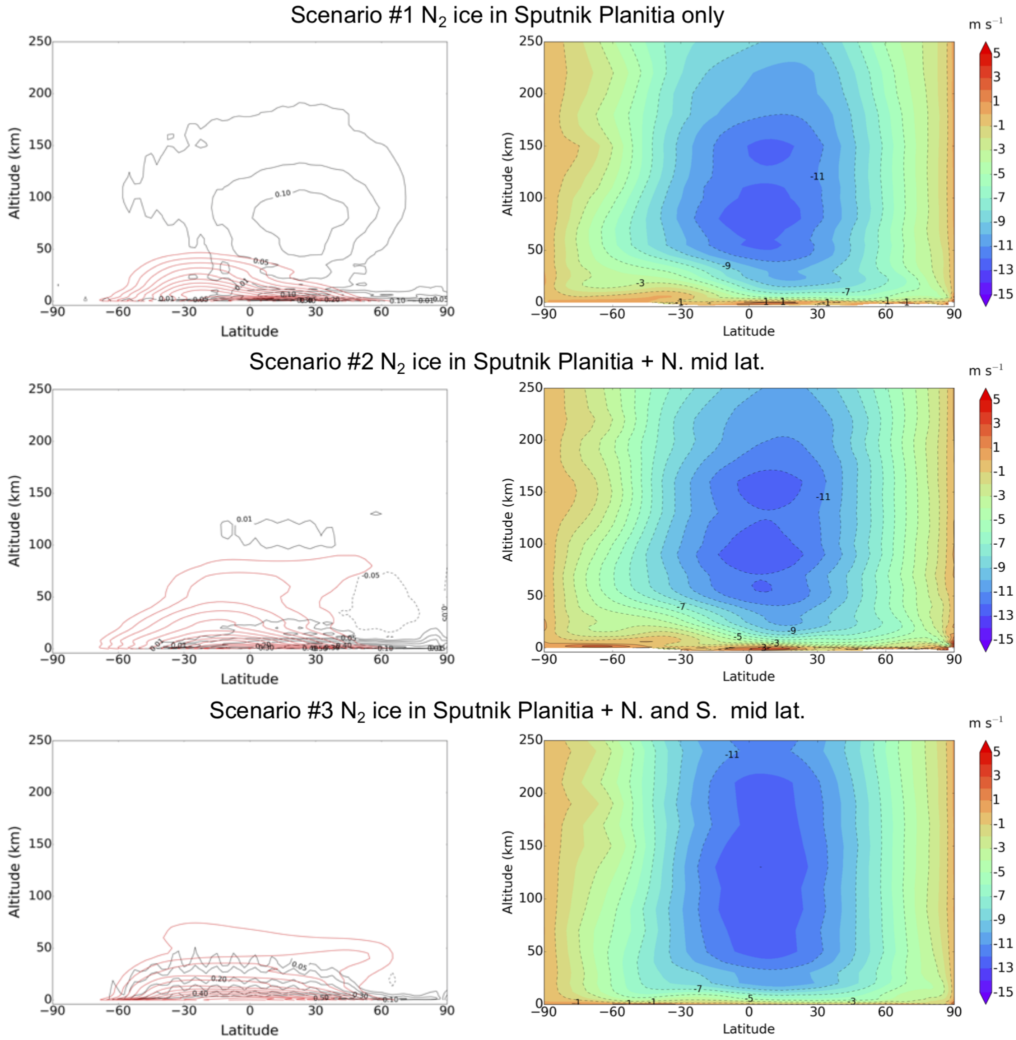

Figure 5. Left column: zonally averaged mass stream functions in units of 10^6 kg s^{-1} (black contour) and angular momentum (red contoured) as obtained for July 2015 in the three GCM simulations explored in this paper. Solid lines denote counterclockwise circulation. Small values of the stream function and angular momentum are not contoured. Note that the streamlines near the surface are not shown as the near-surface winds are strongly and locally impacted by the topography (with mostly katabatic downslope winds) and sublimation-condensation flows. Right column: zonally averaged zonal winds (in m s^{-1}) obtained in the GCM simulations, showing that the general circulation is dominated by retrograde winds in all three cases.

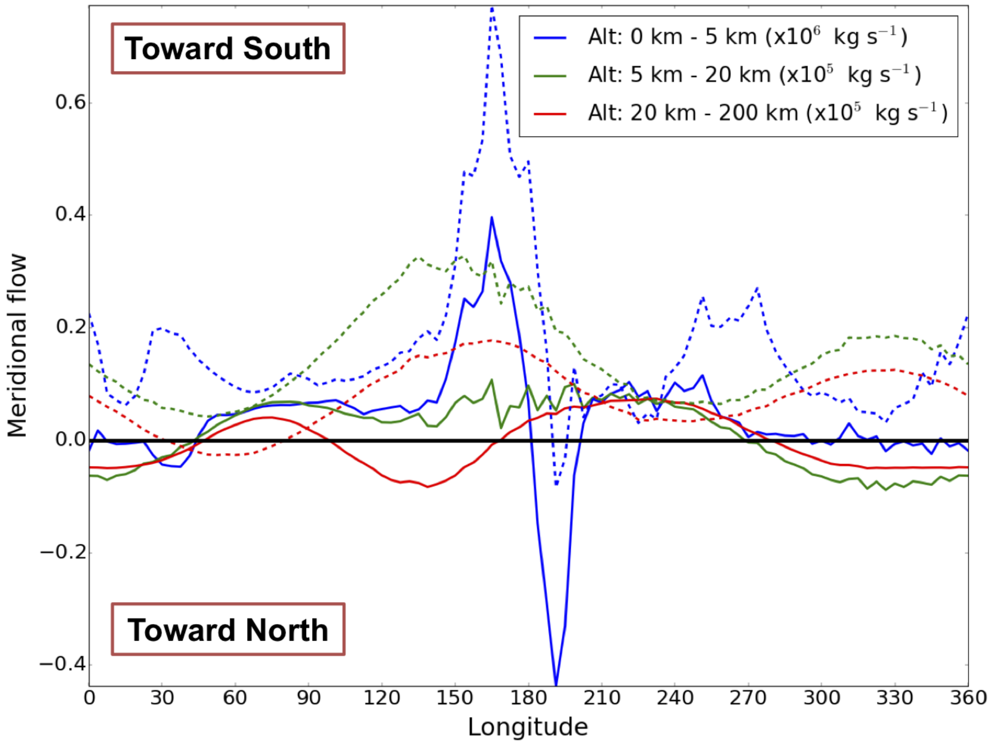

Figure 6. Southward meridional air mass flow averaged between 45°S-45°N for different ranges of altitudes, obtained for GCM scenarios ♯1 (solid lines) and ♯3 (dotted lines).

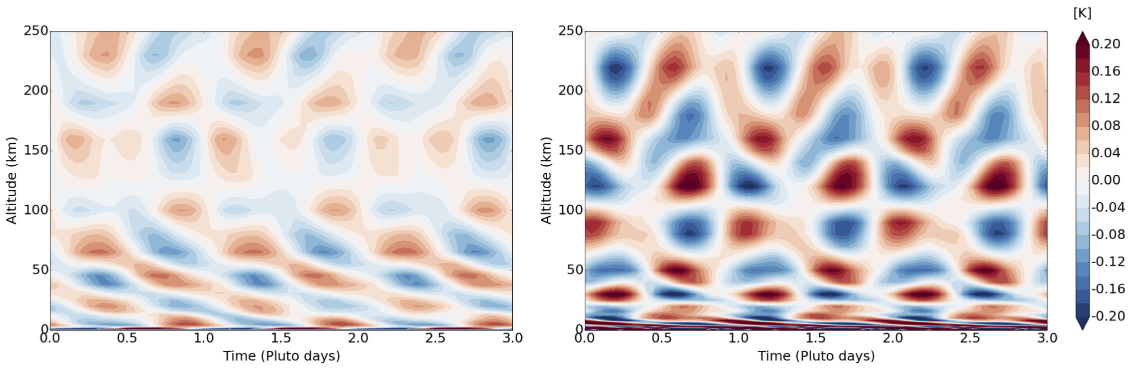

Figure 7. Temperature anomaly (difference between instantaneous value and diurnal average) showing diurnal thermal tides at 0°E-0°N in simulations ♯1 (left) and ♯3 (right) obtained with the GCM in July 2015.

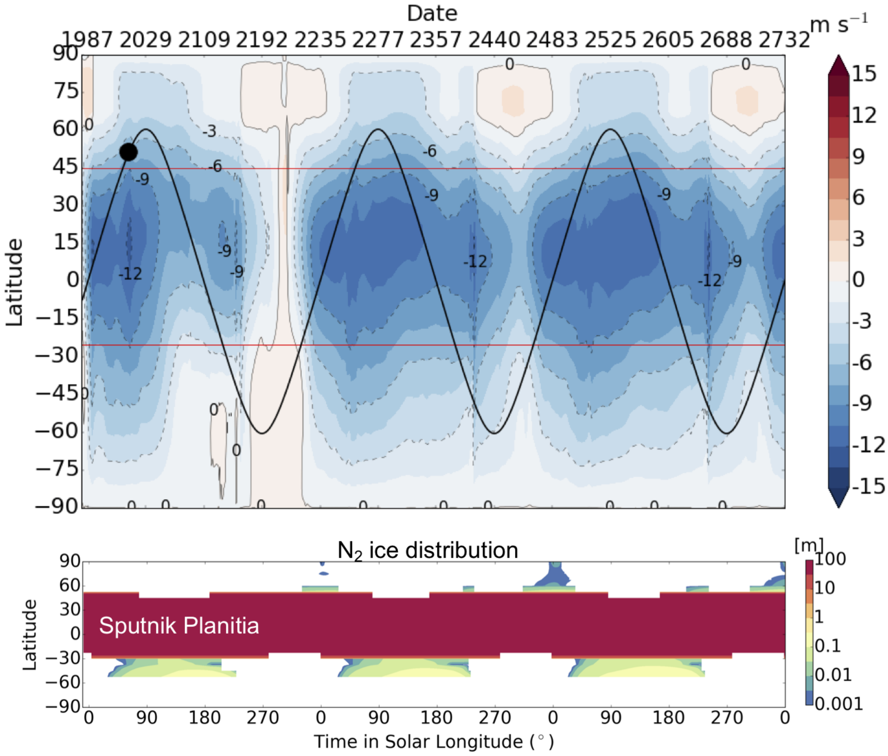

Figure 8. Annual evolution of Pluto's general atmospheric circulation obtained with the GCM. (Top) Zonal mean zonal winds at 20 km above local surface obtained with the 11.25° × 7.5° GCM simulations over one Pluto year. The black solid line indicates the latitude of the subsolar point and its position in 2015 is shown by the black circle. The red horizontal solid lines indicate the bounding latitudes of Sputnik Planitia. The general circulation is dominated by a retro-rotation during most of the year. (Bottom) Zonal mean N_2 ice distribution (Sputnik Planitia is a permanent equatorial km-thick N_2 ice sheet).

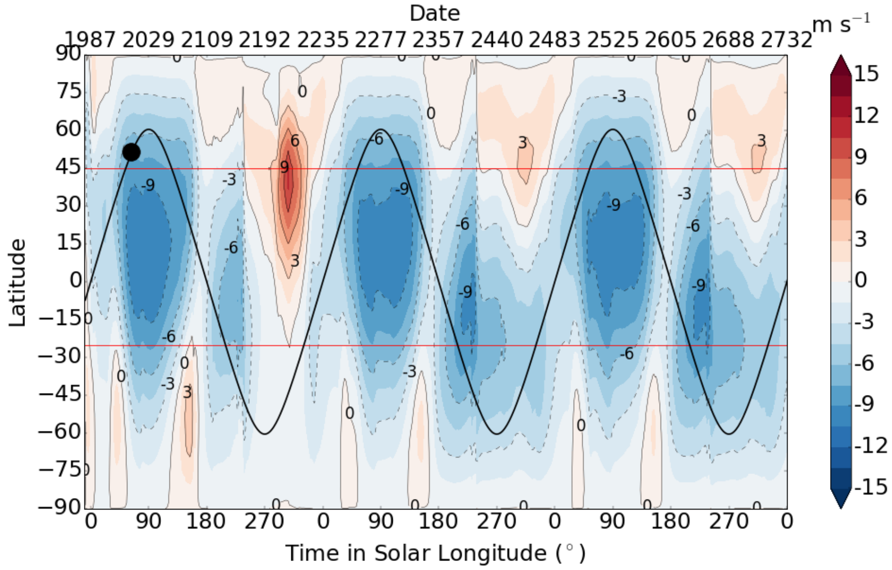

Figure 9. Same as Figure 8, but for an altitude of 100 km above the local surface

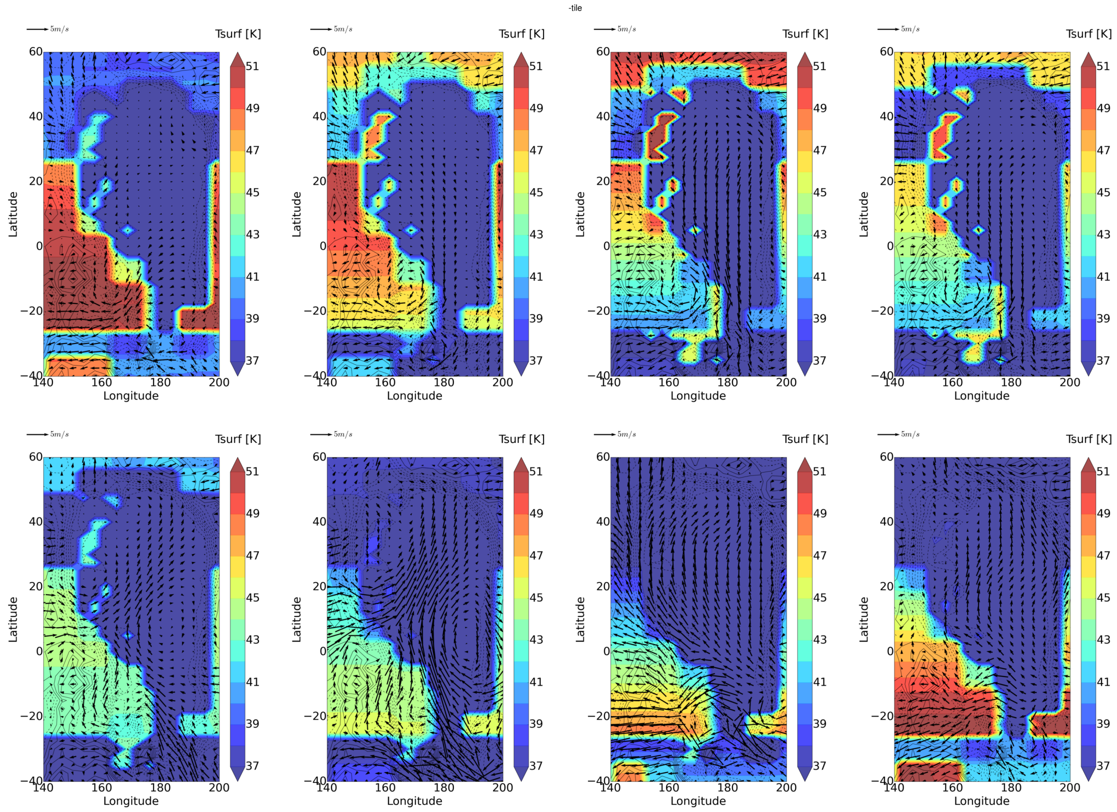

Figure 10. Diurnal mean horizontal winds in Sputnik Planitia obtained with the model at 1000 m above the surface, for L_s = 0°, 45°, 90°, 135° (northern spring and summer, top) and L_s = 180°, 225°, 270° and 315° (northern fall and winter, bottom).

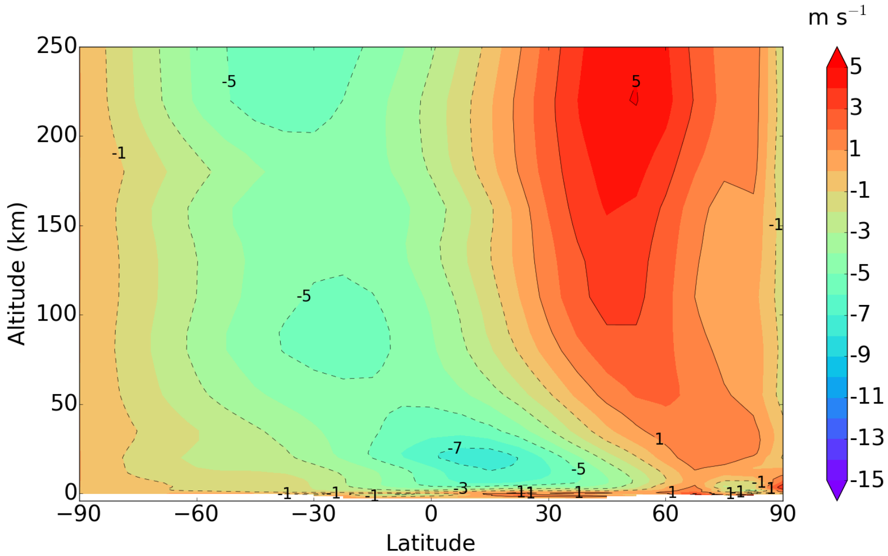

Figure 11. Zonal mean zonal winds obtained at $L_s = 300°$, obtained from the third year of the low resolution GCM simulation, and showing a 5 m s^{-1} prograde jet in the northern hemisphere.

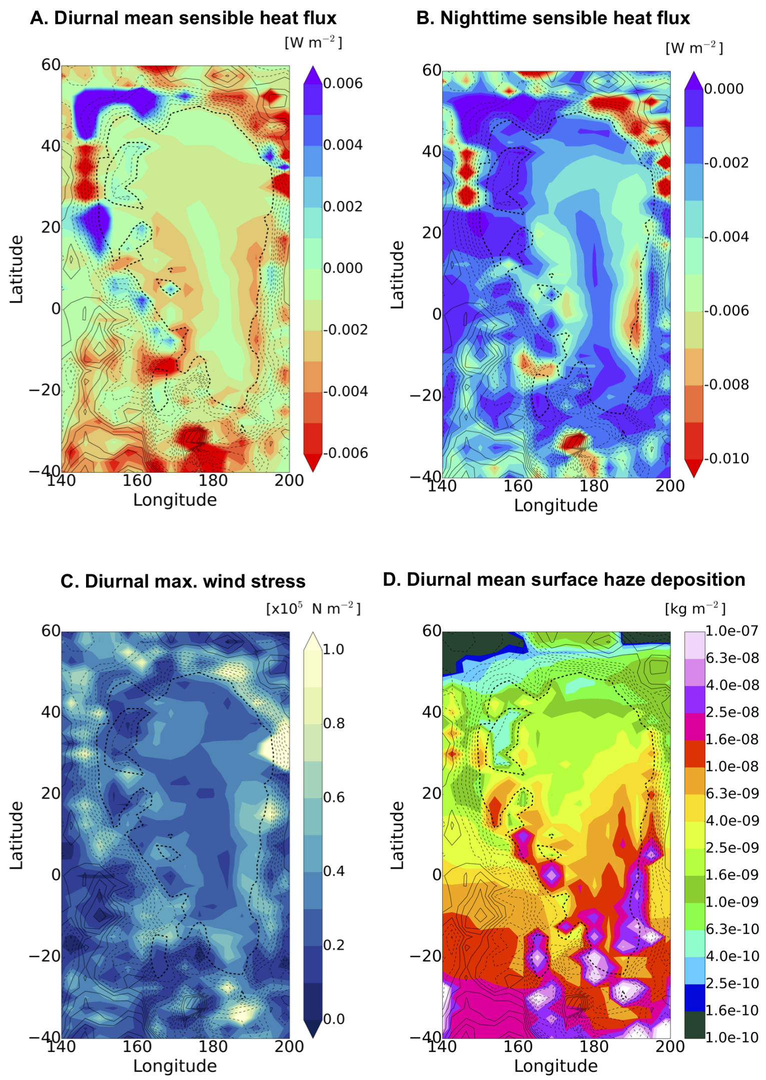

Figure 12. GCM results for 2015: different mechanisms in Sputnik Planitia could explain the contrasts in color and composition observed between the western and central regions of the ice sheet. Topography is contoured (contour interval is 300 m). (A) Diurnal mean sensible heat flux (W m^{-2}), negative values indicate downward flux, limiting the nighttime condensation on N_2 ice . (B) Sensible heat flux averaged during nighttime between 10pm-2am. Sensible heat exchanges are more than one order of magnitude larger over the dark plains than over the bright plains of Sputnik Planitia. (C) Maximal diurnal wind stress on Pluto (N m^{-2}). Higher wind stress values are obtained over the dark plains of Sputnik Planitia. (D) Net surface haze accumulation obtained for one Pluto day in July 2015 (kg m^{-2}).

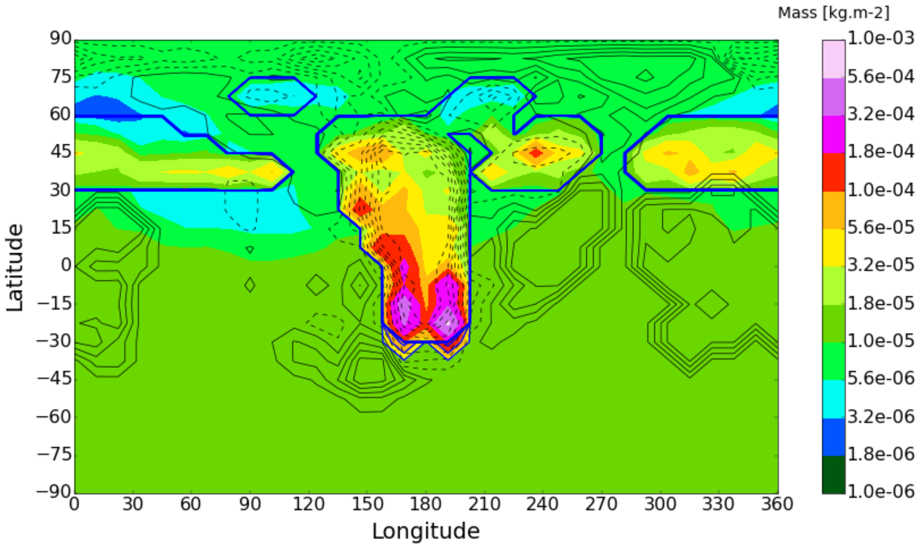

Figure 13. Map of surface haze accumulation (kg m^{-2}) obtained with the low-resolution GCM simulation (scenario ♯2) over the period 1984-2015, assuming 10 nm particles. The blue contours indicate the locations of N_2 ice deposits. The same simulation performed with 100 μm particles (not shown) shows much less contrast of haze accumulation with longitude, because the sedimentation velocity dominates over the winds, which are less efficient at transporting particles around.

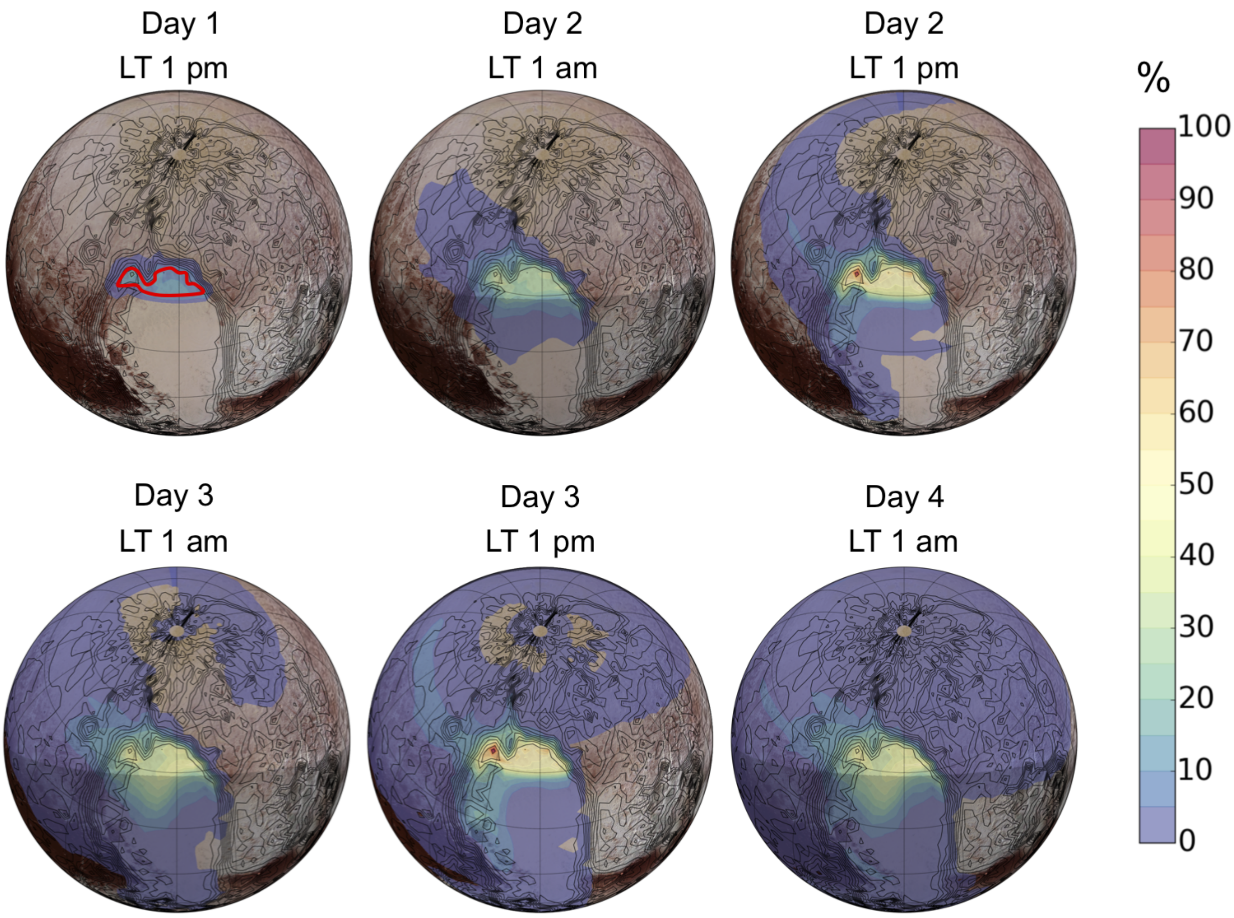

Figure 14. Maps of the atmospheric abundance of dark materials obtained with the GCM during three days following the first injection (snapshots at local times 1 pm and 1 am above Sputnik Planitia). The source of dark materials is indicated by the red line on the first panel. The shading indicates nighttime. The colorbar indicates the fraction of dark materials in the atmosphere to the maximal value obtained over the three days (the value depends on the intensity of the source which is not well constrained).

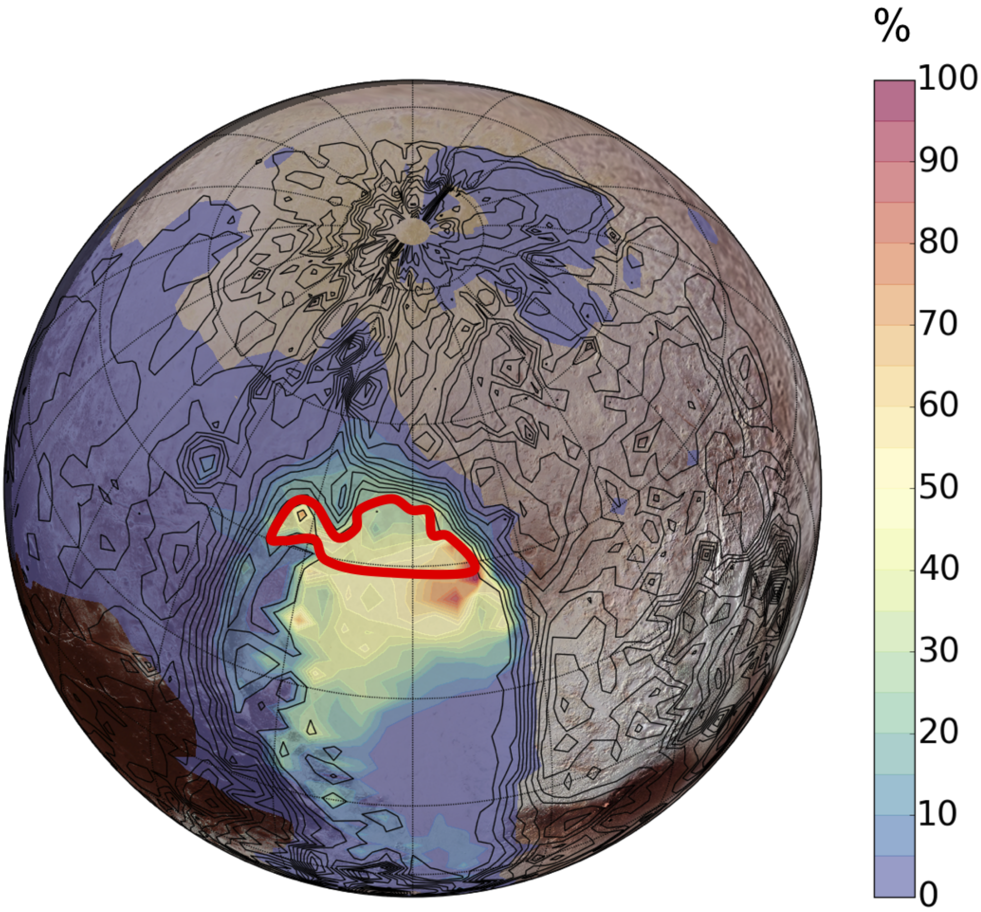

Figure 15. Map of the net surface accumulation of dark materials obtained with the GCM after three days following the first injection (snapshots at local times 1 pm above Sputnik Planitia). A larger amount of dark materials is found in the northern and western regions of Sputnik Planitia. The colorbar indicates the fraction of dark materials in the atmosphere to the maximal value obtained.

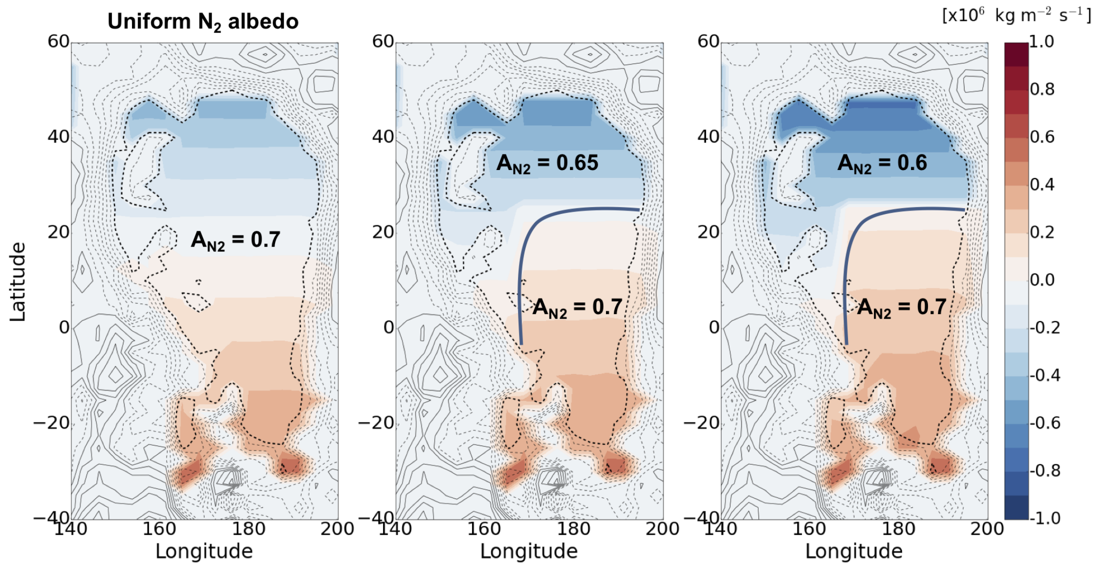

Figure 16. Map of the net diurnal budget of N_2 ice in Sputnik Planitia obtained with the GCM for July 2015, for the reference case using a uniform N_2 ice albedo (left), and for cases using a lower albedo in the northern and western regions (center and right).